RAB1A is a novel vulnerability in uveal melanoma revealed by dual inhibition of MNK1/2 and mTOR.

Raul E. Flores-Gonzalez[1,2], Christophe Goncalves[1], Noah Wirasinghe[1,2], Veronique Gaudreault[3], Jesus M. Noda Ferro[3], Kelly Coutant[4,5], Andrew Mitchell[4], Elizabeth Guettler[1,2], Daniel R. Gonzalez-Moreno[1,2], Samuel Preston[1,2], Feiyang Cai[1,2], Natascha Gagnon[1], Steve Jean[3], Solange Landreville[4,5]*, Wilson H. Miller Jr.[1,2,6]*, Sonia V. del Rincón[1,2,6*]

Affiliations:

[1] *Lady Davis Institute, McGill University*
[2] *Department of Experimental Medicine, McGill University*
[3] *Centre de recherche du CHUS, Université Sherbrooke*
[4] *Centre de Recherche du CHU de Québec-Université Laval*
[5] *Department of Ophthalmology and Otorhinolaryngology-Cervico-Facial Surgery, Université Laval*
[6] *Department of Oncology, McGill University*

[*] To whom correspondence should be addressed:
soniavictoria.delrincon@mcgill.ca

wilson.miller@mcgill.ca

Solange.Landreville@fmed.ulaval.ca

Keywords:

MNK1/2, mTOR, uveal melanoma, RAB1A, liver metastasis. Word Count: 3,581.

Address:
E-504, Lady Davis Institute,
3755 Chemin de la Côte Ste-Catherine,
Room E-504,
Montréal, QC, Canada,
H3T 1E2

ABSTRACT

Uveal melanoma (UM) is an eye cancer that is fatal upon metastasis to the liver. Most treatments trialed in UM fail to provide therapeutic benefit, thus there is an urgent need for novel treatment strategies. The MAPK and PI3K signaling pathways, key molecular drivers found to be hyper-activated in UM, converge on the MNK1/2-eIF4E and mTORC1/2-4EBP axes. Here, we demonstrate that the pharmacologic inhibition of MNK1/2 in combination with an mTOR inhibitor impairs clonogenic outgrowth and UM cell invasion. Proteomic analyses reveal that combined MNK1/2 and mTOR inhibition disrupts Golgi homeostasis and protein vesicle trafficking mainly due to downregulated RAB1A expression, a master regulator of intracellular protein transport. Experimental UM liver metastasis assays show that the knockdown of RAB1A blocks metastasis, a result that is recapitulated by combined pharmacologic inhibition of MNK1/2 and mTOR. This study identifies protein vesicle transport as an unrecognized vulnerability in UM and supports a mechanistic rationale for targeting MNK1/2 and mTOR in metastatic UM.

INTRODUCTION

Uveal Melanoma (UM) is the most common form of primary intraocular cancer in adults, arising from the melanocytes within the uveal tract. Local management of the disease can be achieved with surgery (enucleation or local resection) or radiation therapy, but more than half of patients diagnosed with UM will develop liver metastasis, at which time their 5-year survival rate is estimated to be about 15%[1]. Recent years have seen progress in the treatment of UM, notably with the drug Tebentafusp, with improved overall survival to 21.6 months survival in adults with unresectable or metastatic uveal melanoma, compared to 16.9 months of patients having standard treatment[2]. However, only a small subset of patients (HLA-A*02:01 allele with gp100 melanoma marker) may benefit from receiving Tebentafusp. Patients that do not meet the latter criteria, comprising more than 50% of those with UM, have few to no alternative treatment options[3-6]. As a result, there is a continuous need for new treatment strategies in UM.

Contrary to cutaneous melanoma, UM rarely harbors mutations in *BRAF*[7]; therefore, UM is not treatable with MAPK-targeted therapies as a monotherapy[8]. Instead, two mutually exclusive mutations in *GNAQ* and *GNA11*, which encode the G-protein alpha-subunits that mediate signaling downstream from G-protein-coupled receptors, are present in more than 85% of patient tumors[9]. Mutations in *GNAQ* and *GNA11* result in the constitutive activation of the PI3K and MAPK signaling pathways, which converge on the eIF4F complex, which controls mRNA translation[10,11]. This complex is comprised of eIF4E (5'-cap binding protein), eIF4G (a scaffolding protein) and eIF4A (a DEAD box RNA helicase)[12]. The phosphorylation and availability of eIF4E is tightly controlled. For example, MNK1/2, activated downstream of p38 and ERK MAPK, phosphorylate eIF4E on serine 209, a modification which is critical for the oncogenicity of eIF4E[13]. When phosphorylated, eIF4E increases the translation of a subset of mRNAs coding for proteins involved in cell survival and invasion[14,15]. The availability of eIF4E is regulated by binding to 4E binding proteins (4E-BPs)[16]. In their unphosphorylated form, 4E-BPs bind eIF4E, thus preventing eIF4E from participating in eIF4F complex formation. The phosphorylation of 4E-BPs by activated mTOR frees eIF4E for binding to eIF4G and participate in mRNA translation[17]. Several therapies targeting faulty protein synthesis, including MNK1/2 and mTOR inhibitors, have been or are in clinical trials[18]. Interestingly, mTOR inhibitors, as well as other anti-cancer therapies, increase eIF4E phosphorylation, which may limit their anti-tumor benefit[19-24]. The activation of the MNK1/2-eIF4E axis promotes the translation of metalloproteases (*MMP3*, *MMP9*), transcriptional regulators (*SNAI1*) and survival signals (*MCL1*, *BCL2*) that will result in increased metastatic and proliferative potential. Thus, mTOR inhibitors may be more effective when combined with MNK1/2 inhibitors, which block eIF4E phosphorylation[22]. This concept has been explored in other tumor contexts such as *KRAS*-driven colorectal cancer, chronic myeloid leukemia, and pancreatic cancer[25-27]. MNK1/2 inhibitors such as CGP57380, SEL201 and eFT508 have been shown to reduce tumor progression, clonogenic outgrowth and invasive potential of diverse tumor types[28-31].

We hypothesized that UM are driven, at least in part, by dysregulated mRNA translation. Herein, we show that the MNK and mTOR axes are druggable in human UM. The use of combined small molecule inhibitors targeting MNK and mTOR decreased clonogenic outgrowth and invasion of several UM cell lines. To mechanistically understand how the inhibitors of protein synthesis impact UM, we performed data-independent acquisition mass spectrometry (DIA MS), which, coupled with Metascape and STRING pathway analysis, revealed disruption of vesicular protein trafficking

as a therapeutic vulnerability. We next showed that the small GTPase RAB1A was a downstream target of dual inhibition of MNK and mTOR. In pre-clinical mouse models of UM, genetic repression or overexpression of RAB1A correlated with the presence of liver metastasis. Analysis of publicly available UM patient data (i.e. TCGA-UVM database[32]), showed that patients whose tumors expressed high levels of RAB1A had decreased overall survival, compared to those patients whose tumors expressed low RAB1A. In addition, Class 2 UM samples, i.e. samples most likely to metastasize[33], have higher RAB1A expression when compared to Class 1 UM[34,35]. We also describe that the combination therapy of MNK and mTOR inhibitors decreases metastasis of injected UM cells in an experimental model of liver metastasis. Finally, we demonstrate that targeting RAB1A expression impacts the secretory pathway and reshapes the surfaceome, which may contribute to reduced invasive metastatic potential. Our work reveals RAB1A as a new vulnerability in UM.

RESULTS

The MNK1/2 and mTORC1/2 kinases are active in human UM. MNK1/2 (hitherto MNK) and mTOR are critical regulators of eIF4E phosphorylation and availability, respectively[36]. To determine the activation status of these pathways in primary human UM, we performed immunohistochemistry (IHC) staining on patient-derived UMs, which were arrayed on a tumor microarray (TMA). Using antibodies to detect p-eIF4E and p-S6, downstream targets of MNK and mTOR, respectively, our analysis revealed that most of the UM cores co-expressed p-eIF4E and p-S6 (**Fig. 1a,b** and **Extended Data Fig. 1a**). In addition, we show that tumors expressing high p-eIF4E and p-S6 were from patients who had metastases (**Fig. 1c**). These findings suggest that activated MNK and mTOR signaling may play a role in metastatic disease. Thus, targeting both pathways may provide a therapeutic benefit in a tumor type for which existing therapies are sorely lacking.

Pharmacological inhibition of MNK and mTORC1/2 suppresses clonogenicity and invasion. There is some evidence for the anti-tumor benefit of mTOR inhibitors in preclinical UM models[37], but this did not translate into the clinic setting, where resistance is often observed[37]. One explanation for the limited clinical benefit of mTOR inhibitors such as Sapanisertib (aka INK128)[38], is the increase in the phosphorylation of eIF4E via compensatory feedback mechanisms[19-22]. Accordingly, we hypothesized that therapeutic targeting of mTOR would be more effective when combined with inhibitors of MNK, which block the phosphorylation of eIF4E[22,39]. As expected, INK128 blocked mTOR activity, shown by decreased phosphorylation levels of p-4EBP1 and p-S6. Consistent with previous results, mTOR inhibition led to an increase in eIF4E phosphorylation; however, this effect was mitigated by co-treatment with the MNK inhibitor SEL201 (**Fig. 1d**). We next tested whether the combined inhibition of both axes alters tumor phenotypes in UM. The combination therapy of MNKi+mTORi decreased invasion and clonogenic potential of UM cell lines, as compared to single agent treatments after 24h and 10 days of treatment, respectively (**Fig. 1e,f**). Comparable results were observed in seven additional human UM cell lines (**Extended Data Fig. 2a-c** and **Extended Data Fig. 3a-c**), showing the broad therapeutic benefit of inhibitors of translational control in UM.

Data-independent acquisition mass spectrometry (DIA-MS) uncovered pathways regulated in UM cells treated with combined MNK and mTOR inhibitors. DIA-MS, a quantitative proteomic technique, has been widely used to uncover the mechanisms underlying therapeutic action[40]. DIA-

128 MS provides increased sensitivity, reproducibility and protein coverage, compared with other
129 quantitative LC/MS-MS approaches[41]. We used this proteomic approach to provide insight into the
130 mechanism through which combined MNK and mTOR inhibition represses UM invasion and
131 clonogenic outgrowth. We discovered 326 differentially regulated proteins after 24h of treatment
132 using hierarchical clustering (**Fig. 2a**). Next, we performed pathway enrichment analysis on each
133 cluster (**Extended Data Fig. 4a-f**) while focusing on the proteins being downregulated in the
134 combination treatment (**Fig. 2b**). Particularly, our analysis identified three enriched pathways, two
135 of which are shown to be directly involved in major control of Golgi vesicle trafficking processes
136 comprising membrane organization, vesicle transport and organization (**Fig. 2c**). Among the
137 proteins that are characteristic of these pathways, we noted an overrepresentation of Rab small
138 GTPase family members, such as RAB1A, RAB8A and RAB13 (**Fig. 2d**). Of these, RAB1A was
139 chosen for downstream validation studies, as it was previously shown to play a role in cell
140 migration/invasion in other tumor types, but not in UM[42-45]. Immunoblotting confirmed that
141 RAB1A protein expression was repressed by combined MNK/mTOR inhibitor therapy in T128,
142 T143, 92.1 and MEL290 UM cells after 24 h of treatment (**Fig. 2e**). These cell lines were among
143 those in which we observed robust inhibition of clonogenicity and invasion after combined
144 treatment with MNK1/2 and mTORC1/2 inhibitors (**Fig. 1e,f**).

145 <u>RAB1A is expressed in human UM and correlates with p-S6 and p-4E expression.</u> As the role for
146 RAB1A in UM has not yet been explored, we next interrogated the expression of RAB1A in the
147 TCGA UVM dataset[32], which revealed that increased RAB1A abundance is associated with
148 decreased UM overall survival (**Fig. 2f**). Moreover, our analysis of two publicly available human
149 UM single-cell RNA sequencing data[34,35] showed that Class 2 UM, which have a high propensity
150 to metastasize[46], have the highest expression of RAB1A expression when compared to Class 1 UM
151 (**Fig. 2g**). We next stained the UM TMA described in **Fig. 1a** for RAB1A using IHC and found that
152 RAB1A expression correlated with p-eIF4E and p-S6 expression (**Fig. 2h,i**). Together, these data
153 suggest that RAB1A is expressed in human UM, thereby revealing a novel potential therapeutic
154 vulnerability to block metastasis.

155 <u>RAB1A expression promotes UM invasion and metastasis</u>. To assess whether RAB1A regulates
156 clonogenic outgrowth and invasion, as observed in UM cells treated with combined MNK and
157 mTOR inhibitors, we engineered UM cells to overexpress or silence RAB1A (**Fig. 3a,c,d**).
158 Silencing RAB1A using two approaches, siRNA or shRNA (i.e. RAB1A KD), in T128 and T143,
159 was sufficient to inhibit invasion, similar to the results obtained with the drug combination therapy
160 (**Fig. 3b,e**). In addition, shRNA-mediated knockdown of RAB1A decreased clonogenicity of T128
161 and T143 cells (**Fig. 3f**). Conversely, RAB1A overexpression in T128 and T143 resulted in
162 increased cell invasion and clonogenic outgrowth (**Fig. 3g,h**). We next assessed whether
163 modulation of RAB1A in UM cells would impact liver metastasis, which occurs in more than 90%
164 of patients with UM[1]. We injected empty vector (EV) and RAB1A overexpressing (OE) T128 Luc-
165 tdTomato cells into the spleen of NCG mice, a routinely used model of experimental liver
166 metastasis[47] (**Fig. 4a**). *In vivo* and *ex vivo* imaging revealed higher luminescence, an indicator of
167 greater metastasis burden, in the OE cohort compared to the EV (**Fig. 4b-e**). We confirmed the
168 greater metastasis burden in the mice injected with OE compared to the EV cells by staining the
169 livers with anti-RFP and human nucleolin IHC staining of livers (**Fig. 4f**). We further verified the
170 effect of RAB1A in promoting and suppressing experimental liver metastasis using an additional

171 model: T143 UM cells engineered to silence or overexpress RAB1A, respectively (**Fig. 4g,h**). Our
172 findings reveal that the levels of RAB1A correlate strongly with the presence of liver metastasis.

173 Dual MNK/mTOR pharmacological inhibition decreases UM liver metastasis. To test the *in vivo*
174 impact of combined MNKi-mTORi, T128 luciferase-tdTomato cells were intrasplenically injected
175 into NCG mice (**Fig. 5a**). Drugs were administered by oral gavage 5 days post injection, to test the
176 effect of the inhibitors on metastases already residing in the liver. Bi-weekly *in vivo* imaging of
177 metastasis-bearing animals demonstrated a trend where treatment with SEL201 or INK128 alone
178 decreased the luminescence of the liver compared to the vehicle treatment (**Fig. 5b**). However, only
179 the combination treatment significantly impaired UM outgrowth in the liver, compared to the
180 vehicle control group. The latter was confirmed at endpoint, where *ex vivo* imaging of livers
181 demonstrated that the bioluminescence was decreased in the combination treatment, compared to
182 single agents or vehicle cohorts (**Fig. 5c**). IHC staining of human nucleolin was performed to
183 determine the percentage of human metastasis area within the livers, revealing that the combination
184 treatment robustly decreased the metastasis area compared to the control (**Fig. 5d**). Furthermore,
185 IHC staining revealed the on-target effects of SEL201 and INK128, showing supressed
186 phosphorylation of eIF4E and S6, respectively (**Fig. 5 e,f**). We had predicted that the combination
187 treatment may function to decrease metastatic growth via decreased RAB1A expression, and we
188 indeed found that RAB1A expression was repressed in metastases from the combination treatment
189 arm, thereby supporting our hypothesis (**Fig. 5g**).

190 The ER-to-Golgi secretory pathway is disrupted in RAB1A deficient UM cell lines. Evidence
191 suggests that RAB1A increases the proliferation and invasion of cancer cells via multiple diverse
192 mechanisms[48]. Given that protein trafficking process was one of the pathways highlighted in our
193 proteomic screen, and that RAB1A is known to coordinate ER-to-Golgi vesicle transport, we aimed
194 next to determine whether the secretory pathway was disrupted in shRAB1A expressing UM cells.
195 In eukaryotic cells, newly synthesized proteins transit through the secretory pathway, from the ER
196 to Golgi stacks and finally to the trans-Golgi network (TGN). We employed the Retention Using
197 Selective Hooks (RUSH) system, an assay that helps to synchronize protein secretion and visualize
198 newly synthesized cargos through the secretory pathway[49]. For the RUSH assay, we used the
199 reporter cargo GPI-SBP-eGFP, which is retained in the ER due to the interaction between its
200 streptavidin-binding peptide (SBP) and streptavidin in the hook protein (STR-Li:HA) we used (**Fig.
201 6a**). Upon the addition of biotin to the culture media, the biotin's higher affinity for streptavidin
202 competitively displaces the GPI-SBP-eGFP complex, allowing it to exit the ER and traffic across
203 the secretory pathway. As expected, in the absence of biotin, we detected a similar colocalization
204 of GPI-SBP-eGFP with the ER marker Hook (Li:HA) among the 3 cell lines (**Fig. 6b,d**). We next
205 evaluated the colocalization of GPI-SBP-eGFP cargos with the cis-Golgi GM130 marker at 10, 20,
206 and 30 min after the addition of biotin to monitor the cargo progression through the secretory
207 pathway in pLKO control or shRAB1A T128 cells (**Fig. 6c,e**). We observed that cells with repressed
208 RAB1A expression had a significant decrease in the co-localization of GM130 and GPI-SBP-eGFP
209 cargos to the plasma membrane. These data suggest that upon repression of RAB1A there is
210 impaired trafficking from the Golgi to the plasma membrane (**Fig. 6e,f**).

211 Surfaceome profiling of UM cells with altered RAB1A expression uncovers novel druggable
212 targets. Having determined that the RAB1A expression impacts the secretory pathway, we
213 hypothesized that its expression may also alter plasma membrane-associated proteins. To test this,

214 we examined the surfaceome, which is broadly defined as the subset of proteins expressed on the
215 plasma membrane. We used a quantitative surface biotin-labeling approach coupled with mass
216 spectrometry (**Fig. 7a**) and identified differentially expressed surface proteins in UM cells wherein
217 RAB1A was either knocked down or overexpressed, compared to the respective controls (**Fig. 7b**
218 and **Extended Data Fig. 5a,b**). We performed pathway analysis on the differentially regulated
219 proteins and showed that RAB1A expression influences several signaling pathways previously
220 shown to contribute to invasive and metastatic processes (**Fig. 7c** and **Extended Data Fig. 5c-f**).
221 Among these, 12 proteins were downregulated upon RAB1A knockdown (shRAB1A) and
222 conversely upregulated when RAB1A was overexpressed (RAB1A OE) (**Fig. 7b,d**). We next
223 accessed the TCGA UMV dataset and showed that the identified surface proteins, cell adhesion
224 molecule 1 (CADM1), ephrin type-B receptor 2 (EPHB2), and low-density lipoprotein receptor-
225 related protein 8 (LRP8), positively correlated with RAB1A (**Fig. 7e**), uncovering novel candidate
226 proteins for possible therapeutic intervention in UM. On the contrary, we noted a negative
227 correlation of RAB1A with BAP1, a known tumor suppressor gene in UM. Supporting their
228 potential clinical relevance in UM, we found that high expression of CADM1, EPHB2, and LRP8
229 were significantly associated with poorer overall survival in patients (**Fig. 7f-h**). These findings
230 suggest that RAB1A abundance plays a role in shaping the UM surfaceome, providing potential
231 druggable targets in UM.

232 DISCUSSION

233 The assembly of the eIF4F complex has been shown to be druggable in other tumor contexts and
234 is also the converging point of two major signalling pathways in UM – MAPK and PI3K[31,36]. Our
235 data show that both axes cooperate to enhance metastatic potential and, when inhibited
236 simultaneously, the result is repression of clonogenicity and invasivity *in vitro*, and decreased
237 experimental UM liver metastasis *in vivo*.

238 In this study, we identify RAB1A as a critical downstream effector of activated MNK and mTOR.
239 Other studies have highlighted diverse mechanisms of action associated with the anti-cancer
240 benefits of combined MNK+mTOR inhibition. Teo *et al*. showed that suppression of MNK2
241 (MKI4) and MNK1/2 (MNKI57) with mTOR(rapamycin) resulted in decreased proliferation in
242 leukemic cells, but only observed G1 cell cycle arrest when inhibiting MNK1/2 simultaneously
243 with rapamycin[27]. A similar phenotype was also observed in prostate cancer models, where the
244 inhibition of MNK1/2 (CGP57380) and mTOR together induced G_1 cell cycle arrest due to
245 decreased expression of cyclins A, B, and D1[13]. A recent study by Knight *et al.*, performed in *KRAS*-
246 mutated colorectal cancer, showed robust *in vivo* anti-tumor benefit of combined MNK (eFT508)-
247 mTOR (rapamycin) inhibition, where reducing protein synthesis and blocking p-eIF4E resulted in
248 repressed c-MYC expression[25]. While both our study and Knight *et al*. focused on the tumor-
249 intrinsic effects of MNK1/2 inhibition; numerous studies are emerging that point us to appreciate
250 the role of MNK-eIF4E axis in cells of the tumor microenvironment (TME)[50]. It was shown recently
251 that the MNK-eIF4E axis cooperates with mTOR to shape prostate cancer translatome, producing
252 soluble factors (BGN, SPP1, and HGF) that attract myeloid-derived suppressor cells (MDSCs)[26].
253 Unfortunately, the lack of an immune competent mouse model for UM hinders our ability to
254 characterize the impact of blocking MNK and mTOR on cells of the TME. We anticipate that with
255 such a pre-clinical mouse model in hand, we will be able to expand upon prior work showing that

blocking the MNK-eIF4E axis can potentiate host anti-tumor immunity. For example, the MNK-eIF4E axis can regulate the expression of PD-L1 on cancer cells[51], dendritic cells, and MDSCs[30]. We eagerly await the development of an immune competent model of metastatic UM.

Proper ER to Golgi-mediated protein vesicle trafficking is essential to maintain cell homeostasis, controlling tightly regulated processes such as protein location to the organelles, molecule release to the extracellular compartment[52], internalizing cell membrane receptors and protein degradation via lysosomes[53]. Nevertheless, it can be hijacked by cancer cells to impact the steps in the metastatic cascade such as modifying the tumor microenvironment, aberrant pathway signalization and enhancing oncogenic activity[53,54]. RABs control the major steps of vesicle trafficking by switching from a GDP-inactive to a GTP-active state (mediated by diverse guanine exchange factors [GEFs])[55]. Once GTP bound, RABs will recruit effectors to regulate most steps of vesicular transport, from cargo selection to vesicle budding, transport, tethering and fusion[54,56]. Deregulated cargo delivery and altered RAB family expression can be exploited by cancer cells, where dysregulated vesicle localization triggers metastatic growth[57]. One example is RAB40b, as its localization in secretory vesicles has been shown to be critical for the sorting and transport of MMP2/9. When RAB40b expression is altered, MMPs are directed to lysosomes, resulting in a decreased potential to degrade the extracellular matrix in *in vitro* breast cancer models[58]. Another mechanism by which RABs are hijacked in cancer is the overexpression of RAB25 in radio-resistant lung cancer. The interaction of RAB25 with the EGFR decreased its degradation and enhanced the recycling of the receptor to cell surface in radioresistant lung adenocarcinoma (LUAD)[59]. There are many examples of how RABs have a role in metastatic disease. Although the development of selective inhibitors targeting specific RABs is difficult to achieve due to the close homology among all RAB proteins, the team of Shokat *et al.* recently sought to optimize inhibitors of RAB1A, which may hold promise in UM[60]. Here, we describe that increased RAB1A expression correlates with p-eIF4E and p-S6 in UM and results in decreased patient survival. Moreover, using combined pharmacologic inhibition of MNK and mTOR, we blocked RAB1A expression in *in vitro* and *in vivo* models of UM. Our research, and others, indicate that RAB1A seems to play a crucial role in promoting tumorigenesis, where its overexpression can be used as prognostic marker in colorectal and lung (NSCLC) cancers[43,48,61]. Mechanistically, we showed that when RAB1A expression is decreased, there is a defect in the transport of GPI-SBP-eGFP cargos through the secretory pathway. In our context, we propose that this could lead to altered expression of cell surface proteins, potentially influencing the malignant behavior of cancer cells. Many studies have highlighted the importance of understanding cell surface dynamics in disease progression, particularly how oncogenic kinases such as AKT and MEK drive functional changes that impact invasive and adhesive processes. Some of these alterations can be reversed upon MEK inhibition, highlighting the role of MAPK signaling in surfaceome remodeling[62,63]. Here, using UM cells with genetically manipulated RAB1A expression, we demonstrated that RAB1A abundance influences the expression of CADM1, EPHB2, and LRP8. We then used publicly available data to show a positive correlation of CADM1, EPHB2, and LRP8 with RAB1A, and finally that the expression of those identified plasma membrane-associated proteins was correlated with worse overall survival in UM. Our findings further support previous observations that RAB1A regulates the abundance and location of surface markers at the plasma membrane. Notably, in other contexts, RAB1A influenced migration through integrin β1 recycling and localization to lipid rafts[64]. In a similar

fashion, our results highlight possible novel proteins that may have clinical relevance, suggesting that targeting RAB1A could offer novel therapeutic opportunities in UM.

METHODS

Cell culture: UM cell lines were obtained from Pr. Solange Landreville at Université Laval (Uveal Melanoma Biobank, Vision Sciences Research Network). HEK293FT (Thermo Fisher Scientific, #R70007), T108, T128, T142, and T143 cell lines were cultured in DMEM[65-68] (Wisent, #319-005-CL). 92.1, MEL270, MEL290, MU2, MU2F, OMM2.5 and MP46 were cultured in RPMI 1640[69-71] (Wisent, #350-000-CL). H79 was cultured in DMEM low glucose[72] (Wisent, #319-010 CL). Culture media were supplemented with 10% FBS, 100 IU/mL penicillin and 100 IU/mL streptomycin (Wisent, #450-201-EL) grown at 37°C and 5% CO_2. During experiments, cells were exposed to 2.5 µM SEL201 (RYVU Therapeutics) and 25 nM INK128 (Cayman Chemical). For subculturing or at endpoint, trypsin 1X (WISENT, #325-242-EL) was added after washing with PBS (WISENT, #311-425-CL) followed by addition of 7 mL of complete media to inactivate the trypsin. Cells were spin for 5 min at 240g and resuspended in 3 to 5 mL of complete medium or PBS for downstream experiments.

Colony formation assay: Cells were seeded in 6 well plates at 250 to 2,000 cells per well and allowed to adhere overnight. The medium was changed and drugs added the next day. The medium with drugs was changed every 2 days. At the experimental endpoint, cells were stained with 0.5% crystal violet in 70% ethanol, the plates scanned, and colonies were manually counted using the ImageJ software (https://imagej.net/ij/). For each cell line, we performed at least 3 biological replicates, and 3 triplicates per condition.

Invasion assay: Cells were seeded in a 15 cm petri dish at 1 million cells per plate and allowed to adhere overnight. Cells were starved (serum-free medium) for 16h and then seeded in 12 well plates from 50,000 to 100,000 cells per well in an upper chamber of a polycarbonate insert (8 µm pore size, Corning, # 353182) previously coated with Matrigel (Corning, #354230). At experimental endpoint, the polycarbonate inserts were washed with PBS and cells fixed with 5% glutaraldehyde solution followed by staining with 0.5% crystal violet in 70% ethanol. Non-migratory cells were removed, and invasive cells were counted using EVOS M5000 automatic counting software and manual counting using ImageJ. For each cell line, we performed at least 3 biological replicates, and 3 triplicates per condition. For experiments involving siRNA-mediated knockdown, cells were seeded in 6 well plates at 100,000 cells per well and allowed to adhere overnight. A master mix solution consisting of 3.25 mL of OPTIMEM (Thermo Fisher Scientific, #11058021), 32.5 µL of Lipofectamine RNAiMAX (Invitrogen, #13-778-150) and 6 µL of siRNA targeting *RAB1A* (IDT, siRNA#1 GAUGUCAGGUUUAGUCUUCUGAAGA, siRNA#2 GAUUAUUUAUUCAAGUUACUUCUGA) was prepared, mixed and incubated for 20 min at room temperature. Five hundred uL of the master mix were added to each well along with 2 mL of medium. After 24h, 2 mL of fresh medium were added to each well. Cells were harvested at 48h post-transfection, counted and resuspended in serum-free medium.

Western blotting: A complete protein lysate buffer was prepared using RIPA containing 10 mM Tris (pH 7.4), 1% NP40, 0.1% SDS, 0.1% sodium deoxycholate and 150 mM sodium chloride. Protease and phosphatase inhibitors were added (Roche, #11697498001 and #4906845001) prior to lysing

340 cell pellets. Then, cells were lysed using 50 to 150 uL of complete RIPA and sonicated at 50%
341 power for 4 seconds before centrifuging at 15 000g for 15 min. The protein concentration was
342 measured by Bradford assay (Biorad, #500-0006). Equal levels of proteins were loaded and
343 separated on 10% SDS-PAGE, then transferred into nitrocellulose membranes, and blocked for 1h
344 in 5% non-fat milk dissolved in TBS-T buffer. Membranes were incubated with primary antibodies
345 overnight at 4°C. The next day, membranes were washed with TBS-T buffer and incubated with a
346 secondary antibody for 1h, followed by 3 washes of 10 min with TBS-T. Membranes were
347 developed using Amersham ECL Prime Western Blotting Detection Reagent (Cytiva, #RPN2106)
348 and Immobilon Western Chemiluminescent HRP Substrate (Millipore, #WBKLS0500).

349 Access and reanalysis of previously published data sets. scRNA-seq data were downloaded from
350 the NCBI Gene Expression Omnibus (GEO) public database, accession number GSE139829[35] and
351 GSE138665[34]. RAB1A expression in the uveal melanoma cell population of each patient was
352 further examined after normalization.

353 RAB1A KD and OE cell lines. HEK293FT cells were seeded in a 10 cm petri dish at 2 million cells
354 per plate and allowed to adhere overnight. Cells were transfected with a packaging plasmid
355 (psPAX2), a viral envelope expression plasmid (MD2.G), and either pLKO Control vector or
356 pLKO-shRNA with constructs targeting *RAB1A* (*Homo sapiens* NM_004161.5, TRCN0000157760
357 and TRCN0000280677), or pLX317 control vector and pLX317 RAB1A ORF for gene
358 overexpression of *RAB1A* (*Homo Sapien*s, ORF TRCN0000466775). T128 and T143 UM cell lines
359 were seeded in 10 cm dishes at 1 million cells per dish. The next day, viral particles present in the
360 HEK293FT medium were harvested. A total of 4 mL of medium with viral particles was used to
361 tag the cell lines. Cells were treated with 0.5 ug/mL of puromycin (Sigma, P8833-25MG) to select
362 resistant cells, then further expanded.

363 Luc-tdTomato labeled cell lines. HEK293FT cells were seeded in a 10 cm petri dish at 2 million
364 cells per plate and allowed to adhere overnight. Cells were transfected with a packaging plasmid
365 (psPAX2), an expression plasmid (pCDH-EF1-Luc2-P2A-tdTomato), and a viral envelope
366 expression plasmid (MD2.G). T128 UM cells (pLKO, pLKO-shRNA, pLX317 and pLX317
367 RAB1A OE) were seeded in 10 cm dishes at 1 million cells per dish. The next day, viral particles
368 present in the HEK293FT medium were harvested. A total of 4 mL of medium with 8 µg/mL of
369 polybrene (Sigma, TR-1003-G) with viral particles was used to tag the cell lines. Cells tdTomato+
370 were bulk sorted and expanded.

371 TCGA patient survival analysis. Overall survival data from each patient (N=80, divided in low
372 expressing and high expressing tumors based on RNA expression) were obtained from TCGA-
373 UVM (UCSC Xena Browser) using gene expression dataset. Data for the genes *RAB1A*, *CADM1*,
374 *EPHB2* and *LRP8* were graphed using GraphPad Prism KM survival.

375 Mass spectrometry sample preparation. T128 cells were seeded in a 15 cm petri dish at 2 million
376 cells per plate and allowed to adhere overnight. Cells were treated with inhibitors and harvested at
377 24h post-treatment. We performed 4 biological replicates per treatment. Frozen cell pellets were
378 resuspended in buffer (10 mM HEPES pH 8, 8 M urea), and quantified using BCA assay (Thermo
379 Fisher Scientific, #23225). To reduce disulfide bonds, dithiothreitol (DTT) was added to a final
380 concentration of 5 mM in 50 µg of protein, and samples were heated at 95°C for 2 min. Following

381 a 30-min incubation at room temperature, chloroacetamide (7.5 mM) was added for alkylation, and
382 samples were incubated in the dark for 20 min at room temperature. To dilute the urea concentration
383 to 2 M, 50 mM ammonium bicarbonate (NH_4HCO_3) was added. Peptide digestion was carried out
384 by adding 1 µg of trypsin (Trypsin Gold, Promega) and incubating the samples overnight at 30°C.
385 The reaction was quenched by acidifying the samples to a final concentration of 0.2%
386 trifluoroacetic acid (TFA). An aliquot of the digested peptides was set aside at this stage for DIA
387 spectral library generation. The remaining samples were purified using ZipTip C18 columns (EMD
388 Millipore), lyophilized using a speed vacuum concentrator, and reconstituted in 1% formic acid.
389 The peptide concentration was determined by measuring the absorbance at 205 nm using a
390 NanoDrop spectrophotometer (Thermo Fisher Scientific). Samples were then transferred to glass
391 vials (Thermo Fisher Scientific) and stored at −20°C until mass spectrometry analysis.

392 DIA spectral library preparation. Aliquots set aside for the DIA spectral library were desalted as
393 previously described in the previous section, then dried in a speed vacuum concentrator, and
394 resuspended in 300 µL of 0.1% TFA. Fractionation of the peptide mixture was done using the Pierce
395 High pH Reversed-Phase Peptide Fractionation Kit (Thermo Fisher Scientific). Each fractionation
396 column was first centrifuged at 5,000 × g for 2 min at room temperature to remove excess liquid
397 and to pack the resin. The column was then washed twice with around 300 µL of 100% acetonitrile
398 (ACN) and conditioned with two additional washes of 0.1% TFA. Purified peptides were loaded
399 onto the column, then centrifuged at 3,000 × g for 2 min at room temperature and washed with 300
400 µL of mass spectrometry-grade water. Peptides were sequentially eluted in eight fractions by
401 applying 300 µL of solutions containing 0.1% triethylamine and increasing ACN concentrations
402 (5% to 50%). Each elution step was followed by centrifugation at 3,000 × g for 2 min at room
403 temperature, with fractions collected in separate low-binding microtubes. Fractions were then
404 concentrated to dryness using a speed vacuum concentrator at 60°C and resuspended in 50 µL of
405 1% formic acid (FA). Peptide concentrations were determined by measuring the absorbance at 205
406 nm using a NanoDrop spectrophotometer (Thermo Fisher Scientific). Finally, peptides were
407 transferred to glass vials (Thermo Fisher Scientific) and stored at −20°C until mass spectrometry
408 analysis.

409 DIA LC-MS analysis. For each sample, 250 ng of peptides were injected into the nanoElute high-
410 performance liquid chromatography (HPLC) system (Bruker Daltonics), and later, loaded onto a
411 trap column (Acclaim PepMap100 C18, 0.3 mm ID × 5 mm, Dionex Corporation) with a constant
412 flow rate of 4 µL/min. Peptides were then eluted onto an analytical C18 column (1.9 µm bead size,
413 75 µm × 25 cm, PepSep) using a 2h gradient of ACN from 5% to 37% in 0.1% FA at a flow rate of
414 400 nL/min. Eluted peptides were analyzed using a TimsTOF Pro ion mobility mass spectrometer
415 (Bruker Daltonics) equipped with a Captive Spray nano-electrospray ionization (ESI) source. The
416 data acquisition was performed in data-independent acquisition (DIA) mode using dia-PASEF.
417 Each ion mobility separation cycle (100 ms per trapped ion mobility spectrometry, TIMS, event)
418 was acquired in dia-PASEF mode, with a single mobility window consisting of 27 mass steps per
419 cycle (1.27 s duty cycle). These steps spanned a mass-to-charge ratio (m/z) range of 114 to 1,414
420 with a mass width of 50 Da, covering the diagonal scan line for doubly and triply charged peptides
421 in the m/z-ion mobility plane. The final target intensity was set to 20,000 and intensity threshold of
422 2,500.

423 Protein identification using MaxQuant analysis with TIMS MaxDIA. Mass spectrometry data were
424 analyzed using MaxQuant (version 2.0.3.0) with the UniProt human proteome database (March
425 2020 release, 75,776 entries). The TIMS MaxDIA workflow was applied with all raw files assigned
426 to the same cell type and fractionated from 1 to 8. Trypsin was specified as the digestion enzyme
427 (cleaving after K/R except when followed by P), allowing for one missed cleavage.
428 Carbamidomethylation of cysteine was set as a fixed modification, while methionine oxidation and
429 N-terminal protein modifications were included as variable modifications. A mass tolerance of
430 20 ppm was used for both precursor and fragment ions. To ensure high-confidence identifications,
431 peptide-spectrum matches (PSM FDR), protein identifications (Protein FDR), and site decoy
432 fractions were filtered using a 0.05 false discovery rate (FDR) threshold. A minimum of one peptide
433 was required for protein identification. Additionally, the "Second peptides" and "Match between
434 runs" options were enabled. The analysis was conducted in library mode with a transfer q-value
435 threshold of 0.3, incorporating the "peptides.txt," "evidence.txt," and "msms.txt" files generated
436 from the spectral library. For quantification, label-free quantification (LFQ) normalization was
437 applied across all samples. After identification and normalization, proteins flagged as "Reverse,"
438 "Only identified by site," or "Potential contaminant" were excluded. Proteins detected by a single
439 unique peptide were also removed from further analysis.

440 MS data analysis for LFQ-MS. LFQ relative intensities obtained from MaxQuant were processed
441 for statistical analysis. PERSEUS software was used to perform multiple hypothesis testing using
442 two-sided Student's t-test and permutation-based FDR correction of 10%. Significant
443 up/downregulated proteins were normalized and hierarchically clustered. Pathway analyses were
444 performed for each cluster using Metascape to determine the effect of the drug combination on
445 specific pathways.

446 Splenic injection model. Six-week-old NCG mice (Charles River Laboratories) were injected in
447 the spleen with 100,000 T143 or T128 luc-tdTomato cells resuspended in PBS to induce metastasis
448 in the liver. Splenectomy was performed only in cohorts treated with vehicle or SEL201 and
449 INK128. Mice were imaged using AMI HT (Spectral Imaging) by injecting 200 uL of luciferin
450 (15 mg/mL) (PerkinElmer, #122799) dissolved in sterile PBS weekly or bi-weekly to tract
451 metastatic growth. At the endpoint, mice were euthanized, the liver and lungs were harvested and
452 fixed in 10% formalin before paraffin embedding for IHC assays. Surface liver metastases were
453 visually quantified for T143 mice cohorts the day after euthanasia.

454 TMA IHC and scoring. Cores from human primary UM FFPE tissues were acquired from 18
455 patients and arranged/mounted in a TMA. Only 11 patient cores had sufficient tissue to be analyzed.
456 Four-µm TMA sections were stained for p-eIF4E, p-S6, and RAB1A using IHC (see below). Cores
457 were scored using the following metric: low, medium, or high expression, based on the overall cell
458 intensity signal quantified using the QuPath software (https://qupath.github.io/). For p-eif4E, a low
459 score corresponded to an intensity range of 0 to 0.1, medium score ranged from 0.1 to 0.16, and
460 high score was above 0.16. For p-S6, low score ranged from 0 to 0.125, medium score from 0.125
461 to 0.22, and high score was above 0.22. For RAB1A, low score ranged from 0 to 0.12, medium
462 score from 0.12 to 0.23, and high score was above 0.23. Correlation was determined using a
463 Spearman's test. Red fluorescent protein (RFP) and RAB1A stainings were performed in murine
464 liver tissues. Metastatic UM cells expressing tdTomato were quantified using QuPath. The
465 metastasis area was calculated by dividing area covered by metastases over total liver tissue area.

466 IHC on livers bearing UM metastases. NCG mouse livers were collected, washed with 1X PBS,
467 and fixed in 10% neutral buffered formalin (VWR, # 89370-094). Samples were then embedded in
468 paraffin, sectioned at a thickness of 4 µm, and mounted on Superfrost slides. IHC staining was
469 conducted on liver tissues containing metastases. Slides underwent deparaffinization, rehydration,
470 and heat-induced antigen retrieval. To inhibit endogenous peroxidase activity, the tissues were
471 treated with 10% hydrogen peroxide for 15 min, followed by blocking with 10% donkey serum
472 (Jackson ImmunoResearch, #017-000-121). The primary antibody staining was performed using
473 nucleolin (metastases; 1:2,000 dilution), p-eIF4E (metastasis-bearing livers; 1:50 dilution), p-S6
474 (metastasis-bearing livers; 1:200 dilution), and RAB1A (1:100 dilution). The Magenta substrate
475 (Agilent, #GV92511-2) or the ImmPACT DAB substrate (Vector Laboratories, #SK-4105) was
476 used for visualization with Harris-modified hematoxylin (EMD Millipore, #638A-85) as the
477 counterstain. Images of the stained slides were captured using a Zeiss AxioScan.Z1 slide scanner
478 and analyzed with the QuPath software.

479 Retention Using Selective Hooks (RUSH) assay. T128 cells were cultured in DMEM supplemented
480 with 10% FBS and pen/strep with 2ug/ml of puromycin. Cells were detached with trypsin + 0.25%
481 EDTA and a total of $3x10^4$ cells were plated on round glass coverslips (72230-01; Electron
482 Microscopy Sciences) in a 24-well plate. Cells were allowed to adhere for 48 h before being
483 transfected with 500 ng of Ii-Str_SBP-EGFP-GPI plasmid (65296, Addgene) using JetPRIME
484 reagent (101000046; Polyplus), as per the manufacturer's instructions. The transfection media was
485 removed 7 h later and replaced with Opti-Minimal Essential Medium (MEM) supplemented with
486 2% FBS. Twenty-four hours after the transfection and 1h before the RUSH assay, the culture
487 medium was replaced with DMEM supplemented with 10% of dialyzed FBS, to limit the amount
488 of biotin in the medium. The RUSH assay was initiated by replacing the culture medium with
489 DMEM supplemented with 10% dialyzed FBS and 40 µM of biotin. Cells were incubated at 37°C
490 for 0, 10, 20 or 30 min. Plates were then lifted on ice and medium was quickly replaced by ice-cold
491 PBS. Cells were fixed for 15 min at room temperature with 4% paraformaldehyde (Electron
492 Microscopy Science, #15713) in PBS, and then incubated for 1h at room temperature in PBS
493 containing 0.3% Triton X-100 and 1% bovine serum albumin (BSA). Two sets of cells incubated
494 without the addition of biotin during the RUSH assay (time 0) were labelled to identify different
495 proteins. The first set was stained with anti-HA (1:800; Cell Signaling, #3724), anti-GFP (1:1,000;
496 Santa Cruz Biotechnology, #sc-9996) and DAPI to evaluate the colocalization of the cargo and
497 hook. The second set was stained with the rest of the RUSH assay samples with anti-GM130
498 (1:3,000; Cell Signaling, #12480), anti-GFP and DAPI to evaluate the colocalization of the cargo
499 and cis-Golgi. Secondary antibodies used were Alexa-Fluor 488-conjugated anti-mouse and Alexa-
500 Fluor 546-conjugated anti-rabbit (1:400; Invitrogen, #A11029 and #A11035). Cells were mounted
501 on slides with 3 µL of slow fade gold mounting medium containing DAPI (Thermo Fischer
502 Scientific, #S36938). Slides were kept at 4°C in the dark before image acquisitions on a Zeiss
503 LSM880 equipped with a 40x 1.4 plan Apo objective. Images were exported as tiff files using Zen
504 Blue, and then processed using Adobe Photoshop. All images were thresholded and cropped
505 similarly in Photoshop for the experimental set. Figures were assembled using Adobe Illustrator.
506 The image analysis was performed using Cell Profiler (https://cellprofiler.org/). Pearson
507 coefficients were calculated per cell using the colocalization module. All experiments were
508 performed three times independently. The colocalization of the cargo and hook at time 0 was
509 statistically compared between cell types using a Kruskal-Wallis test followed by Dunn's multiple

comparison test. The colocalization of the cargo and Golgi at the 4 tested time points was analyzed by a two-way ANOVA followed by Dunnett's post-test.

Surface labeling. Solutions and cell plates were prechilled at 4°C, and all steps were performed on ice to prevent the internalization of membrane proteins. Cells were washed twice with Buffer A (0.5 mM $MgCl_2$, 1 mM $CaCl_2$ in 1X PBS, pH 7.4) and then incubated for 30 min at 4°C in the dark with 1 mM sodium metaperiodate (Sigma-Aldrich, #S1878-25G) dissolved in Buffer A. Subsequently, cells were washed twice with cold Buffer A and incubated for 1h at 4°C in the dark with 100 µM aminooxy-biotin (Biotium Inc., #90113) and 10 mM aniline (Sigma-Aldrich, #242284) for biotinylation. Cells were washed twice again with Buffer A and gently scraped off the plate surface with lysis buffer containing a protease inhibitor cocktail (Sigma-Aldrich, #P8340). The lysate was gently rocked at 4°C for 30 min, and vortexed every 5 min. Nuclei and cell debris were removed by centrifugation at 2,800 × g for 15 min, followed by 16,000 × g for 15 min. The supernatant was collected for membrane protein isolation with high-capacity streptavidin resin (Thermo Fisher Scientific, #20357).

Sample preparation and mass spectrometry analysis. After several harsh washes (see complementary protocol), streptavidin beads were washed five times with 20 mM ammonium bicarbonate. Proteins bound to beads were reduced with 10 mM DTT in 20 mM NH_4HCO_3 and alkylated with 15 mM chloroacetamide in 20 mM NH_4HCO_3. The digestion was carried on overnight at 37°C with 1 µg of trypsin (Thermo Fisher Scientific, #PI90058). Beads were finally centrifugated and the supernatant containing the peptides was collected. The peptide mixture was dried and resuspended in 300 µL of 0.1% TFA to subsequent desalting on ZipTip micropipette tips containing a C18 resin (EMD Millipore). The MS analysis was performed by diaPASEF technique implemented in the timsTOF from Bruker Daltonics. For each sample, 250 ng of the desalted peptide mixtures were analyzed by a LC-MS system (nanoElute, Bruker Daltonics), with diaPASEF on a timsTOF Pro ion mobility mass spectrometer. Peptides were loaded onto a trap column (Acclaim PepMap100 C18 column, 0.3 mm inner diameter × 5 mm, Dionex Corporation) at a flow rate of 4 µL/min and moved to an analytical C18 column (1.9 µm particle size, 75 µm x 25 cm; PepSep) maintained at 50°C. Then, peptides were eluted over 120 min gradient time (ACN (5%–37%) in 0.1% FA at 400 nL/min) and injected into the Captive Spray nano electrospray source of TimsTOF Pro (Bruker Daltonics). In diaPASEF mode, a mobility window consisting of 27 mass steps (m/z between 114 to 1,414 with a mass width of 50 Da) per cycle (1.27 seconds duty cycle) was used. Peptides carrying +2 and +3 charges were selected for analysis.

MS data analysis. Protein identification was performed with DIA-NN (version 1.9.1). *In silico* spectral libraries were created using the Human FASTA file (one protein per gene) from the UniProt database, with Proteome ID UP000005640 and the universal protein contaminant FASTA file available on the repository (https://github.com/HaoGroup-ProtContLib; Frankenfield *et al.*, 2022). Deep learning-based spectra, RTs and IMs prediction option, as well as N-terminal M excision, C(cam) and M(ox) modifications were enabled. Moreover, trypsin/P was selected allowing two missed cleavages and the precursor charge range was set to 2+ and 3+. Bruker.d raw data were analyzed by searching against the generated libraries.

Differential expression analysis. Membrane proteins were selected by their accession numbers on UniProt. A total of 846 membrane proteins were identified with DIA-NN. Differential expression

552 analysis (DEA) between biological conditions was achieved using the open-source R package Mass
553 Spectrometry Downstream Analysis Pipeline (MS-DAP). This package allows the analysis of label-
554 free proteomics datasets from the DIA-NN tool. MS-DAP incorporates statistical models for DEA
555 like MSqRob (Goeminne *et al.*, 2016) and MS-EmpiRe (Ammar *et al.*, 2019) that work directly at
556 the peptide level. These novel statistical models are more sensitive in detecting small variations
557 (20-25% change) in peptide abundances, rather than averaging all values into a single protein
558 estimate (as Perseus).

559 Defining statistically significant hits. Peptide-level-based models increase sensitivity for detecting
560 differentially expressed proteins but may also inflate false positives. To address this, DEA results
561 were initially restricted to proteins identified with at least two peptides. Furthermore, instead of
562 applying an arbitrary log2 fold change threshold, statistically significant hits were defined
563 automatically through bootstrapping analyses using MS-DAP. This combination of restrictions has
564 been shown to effectively control false positive rates. Finally, all differentially expressed proteins
565 were filtered to retain only proteins with a q-value < 0.01 (Benjamini-Hochberg method).

566 ACKNOWLEDGMENTS

567 This research was funded by the Canadian Institutes of Health Research (CIHR) (grants PJT-
568 178194 to SVDR & SL, grant PJT-183934 to WHM, and grant PJT-518272 to SJ) and a grant from
569 the CRS-Liver Foundation and CIHR to SVDR. Further funding was provided by the Samuel
570 Waxman Cancer Research Foundation. Procurement of UM cells was possible thanks to the
571 common infrastructure "Uveal Melanoma Biobank", which is financially supported by the Fonds
572 de recherche du Québec - Santé (FRQS)-Vision Sciences Research Network (VSRN; SL). SL is a
573 Junior 2 Research Scholar of the FRQS. REFG, FC, and SP were funded by FRQS doctoral
574 scholarships. KC was supported by doctoral training awards from Mitacs, the VSRN, the Eye
575 Disease Foundation, the Fondation du CHU de Québec-Desjardins, the Centre de recherche sur le
576 cancer de l'Université Laval, and the Centre de recherche en organogénèse expérimentale de
577 l'Université Laval/LOEX. The authors wish to extend their gratitude to Mr. Christian Young,
578 manager of the Flow Cytometry Core facility at the Lady Davis Institute and Dr. Naciba Benlimame
579 of the Molecular Pathology Core of the JGH, for their technical support. We express our
580 appreciation to Mrs. Véronique Michaud and Mrs. Kathy Ann Forner for their aid into developing
581 our animal models. We acknowledge the technical support of the Lady Davis Institute for Medical
582 Research Imaging and Phenotyping Core. We are grateful for the support from Mr. Marc Bazin, the
583 platform manager of the In Vivo Imaging System Lumina (Centre de recherche du CHU de Québec-
584 Université Laval), for its collaboration to acquire luminescent images.

585 REFERENCES

586 1 Park, J. J. *et al.* Oncogenic signaling in uveal melanoma. *Pigment Cell Melanoma Res* **31**, 661-672
587 (2018). https://doi.org/10.1111/pcmr.12708
588 2 Di Leo, L., Bodemeyer, V. & De Zio, D. The Complex Role of Autophagy in Melanoma Evolution:
589 New Perspectives From Mouse Models. *Front Oncol* **9**, 1506 (2019).
590 https://doi.org/10.3389/fonc.2019.01506
591 3 Triozzi, P. L. & Singh, A. D. Adjuvant Therapy of Uveal Melanoma: Current Status. *Ocul Oncol*
592 *Pathol* **1**, 54-62 (2014). https://doi.org/10.1159/000367715

4 Middleton, M. R. *et al.* Tebentafusp, A TCR/Anti-CD3 Bispecific Fusion Protein Targeting gp100, Potently Activated Antitumor Immune Responses in Patients with Metastatic Melanoma. *Clin Cancer Res* **26**, 5869-5878 (2020). https://doi.org/10.1158/1078-0432.Ccr-20-1247

5 Olivier, T., Haslam, A., Tuia, J. & Prasad, V. Eligibility for Human Leukocyte Antigen-Based Therapeutics by Race and Ethnicity. *JAMA Netw Open* **6**, e2338612 (2023). https://doi.org/10.1001/jamanetworkopen.2023.38612

6 Souri, Z., Wierenga, A. P. A., Mulder, A., Jochemsen, A. G. & Jager, M. J. HLA Expression in Uveal Melanoma: An Indicator of Malignancy and a Modifiable Immunological Target. *Cancers (Basel)* **11** (2019). https://doi.org/10.3390/cancers11081132

7 Maleka, A., Åström, G., Byström, P. & Ullenhag, G. J. A case report of a patient with metastatic ocular melanoma who experienced a response to treatment with the BRAF inhibitor vemurafenib. *BMC Cancer* **16**, 634 (2016). https://doi.org/10.1186/s12885-016-2657-7

8 Hitchman, T. D. *et al.* Combined Inhibition of Gα(q) and MEK Enhances Therapeutic Efficacy in Uveal Melanoma. *Clin Cancer Res* **27**, 1476-1490 (2021). https://doi.org/10.1158/1078-0432.Ccr-20-2860

9 Van Raamsdonk, C. D. *et al.* Mutations in GNA11 in uveal melanoma. *N Engl J Med* **363**, 2191-2199 (2010). https://doi.org/10.1056/NEJMoa1000584

10 Yang, J., Manson, D. K., Marr, B. P. & Carvajal, R. D. Treatment of uveal melanoma: where are we now? *Ther Adv Med Oncol* **10**, 1758834018757175 (2018). https://doi.org/10.1177/1758834018757175

11 Kujala, E., Mäkitie, T. & Kivelä, T. Very long-term prognosis of patients with malignant uveal melanoma. *Invest Ophthalmol Vis Sci* **44**, 4651-4659 (2003). https://doi.org/10.1167/iovs.03-0538

12 Topisirovic, I., Svitkin, Y. V., Sonenberg, N. & Shatkin, A. J. Cap and cap-binding proteins in the control of gene expression. *Wiley Interdiscip Rev RNA* **2**, 277-298 (2011). https://doi.org/10.1002/wrna.52

13 Bianchini, A. *et al.* Phosphorylation of eIF4E by MNKs supports protein synthesis, cell cycle progression and proliferation in prostate cancer cells. *Carcinogenesis* **29**, 2279-2288 (2008). https://doi.org/10.1093/carcin/bgn221

14 Furic, L. *et al.* eIF4E phosphorylation promotes tumorigenesis and is associated with prostate cancer progression. *Proc Natl Acad Sci U S A* **107**, 14134-14139 (2010). https://doi.org/10.1073/pnas.1005320107

15 Topisirovic, I., Ruiz-Gutierrez, M. & Borden, K. L. Phosphorylation of the eukaryotic translation initiation factor eIF4E contributes to its transformation and mRNA transport activities. *Cancer Res* **64**, 8639-8642 (2004). https://doi.org/10.1158/0008-5472.Can-04-2677

16 Alain, T. *et al.* eIF4E/4E-BP ratio predicts the efficacy of mTOR targeted therapies. *Cancer research* **72**, 6468-6476 (2012). https://doi.org/10.1158/0008-5472.CAN-12-2395

17 Fan, S., Li, Y., Yue, P., Khuri, F. R. & Sun, S. Y. The eIF4E/eIF4G interaction inhibitor 4EGI-1 augments TRAIL-mediated apoptosis through c-FLIP Down-regulation and DR5 induction independent of inhibition of cap-dependent protein translation. *Neoplasia* **12**, 346-356 (2010). https://doi.org/10.1593/neo.10144

18 Li, S., Chen, J.-s., Li, X., bai, X. & Shi, D. MNK, mTOR or eIF4E-selecting the best anti-tumor target for blocking translation initiation. *European Journal of Medicinal Chemistry* **260**, 115781 (2023). https://doi.org/https://doi.org/10.1016/j.ejmech.2023.115781

19 Adesso, L. *et al.* Gemcitabine triggers a pro-survival response in pancreatic cancer cells through activation of the MNK2/eIF4E pathway. *Oncogene* **32**, 2848-2857 (2013). https://doi.org/10.1038/onc.2012.306

20 Sun, S. Y. *et al.* Activation of Akt and eIF4E survival pathways by rapamycin-mediated mammalian target of rapamycin inhibition. *Cancer Res* **65**, 7052-7058 (2005). https://doi.org/10.1158/0008-5472.Can-05-0917

642 21 Astanehe, A. *et al.* MKNK1 is a YB-1 target gene responsible for imparting trastuzumab resistance
643 and can be blocked by RSK inhibition. *Oncogene* **31**, 4434-4446 (2012).
644 https://doi.org/10.1038/onc.2011.617
645 22 Altman, J. K. *et al.* Inhibition of Mnk kinase activity by cercosporamide and suppressive effects on
646 acute myeloid leukemia precursors. *Blood* **121**, 3675-3681 (2013). https://doi.org/10.1182/blood-
647 2013-01-477216
648 23 Prabhu, S. A. *et al.* Inhibition of the MNK1/2-eIF4E Axis Augments Palbociclib-Mediated
649 Antitumor Activity in Melanoma and Breast Cancer. *Mol Cancer Ther* **22**, 192-204 (2023).
650 https://doi.org/10.1158/1535-7163.Mct-22-0092
651 24 Pham, T. N. D. *et al.* Induction of MNK Kinase-dependent eIF4E Phosphorylation by Inhibitors
652 Targeting BET Proteins Limits Efficacy of BET Inhibitors. *Mol Cancer Ther* **18**, 235-244 (2019).
653 https://doi.org/10.1158/1535-7163.Mct-18-0768
654 25 Knight, J. R. P. *et al.* MNK Inhibition Sensitizes KRAS-Mutant Colorectal Cancer to mTORC1
655 Inhibition by Reducing eIF4E Phosphorylation and c-MYC Expression. *Cancer Discov* **11**, 1228-
656 1247 (2021). https://doi.org/10.1158/2159-8290.Cd-20-0652
657 26 Brina, D. *et al.* The Akt/mTOR and MNK/eIF4E pathways rewire the prostate cancer translatome
658 to secrete HGF, SPP1 and BGN and recruit suppressive myeloid cells. *Nat Cancer* **4**, 1102-1121
659 (2023). https://doi.org/10.1038/s43018-023-00594-z
660 27 Teo, T. *et al.* Pharmacologic co-inhibition of Mnks and mTORC1 synergistically suppresses
661 proliferation and perturbs cell cycle progression in blast crisis-chronic myeloid leukemia cells.
662 *Cancer Lett* **357**, 612-623 (2015). https://doi.org/10.1016/j.canlet.2014.12.029
663 28 Guo, Q. *et al.* MNK1/NODAL Signaling Promotes Invasive Progression of Breast Ductal
664 Carcinoma In Situ. *Cancer Res* **79**, 1646-1657 (2019). https://doi.org/10.1158/0008-5472.Can-18-
665 1602
666 29 Zhan, Y. *et al.* MNK1/2 inhibition limits oncogenicity and metastasis of KIT-mutant melanoma. *J*
667 *Clin Invest* **127**, 4179-4192 (2017). https://doi.org/10.1172/jci91258
668 30 Huang, F. *et al.* Inhibiting the MNK1/2-eIF4E axis impairs melanoma phenotype switching and
669 potentiates antitumor immune responses. *J Clin Invest* **131** (2021).
670 https://doi.org/10.1172/jci140752
671 31 Prabhu, S. A., Moussa, O., Miller, W. H., Jr. & Del Rincón, S. V. The MNK1/2-eIF4E Axis as a
672 Potential Therapeutic Target in Melanoma. *Int J Mol Sci* **21** (2020).
673 https://doi.org/10.3390/ijms21114055
674 32 Weinstein, J. N. *et al.* The Cancer Genome Atlas Pan-Cancer analysis project. *Nat Genet* **45**, 1113-
675 1120 (2013). https://doi.org/10.1038/ng.2764
676 33 Bergeron, M. A., Champagne, S., Gaudreault, M., Deschambeault, A. & Landreville, S. Repression
677 of genes involved in melanocyte differentiation in uveal melanoma. *Mol Vis* **18**, 1813-1822 (2012).
678 34 Pandiani, C. *et al.* Single-cell RNA sequencing reveals intratumoral heterogeneity in primary uveal
679 melanomas and identifies HES6 as a driver of the metastatic disease. *Cell Death Differ* **28**, 1990-
680 2000 (2021). https://doi.org/10.1038/s41418-020-00730-7
681 35 Durante, M. A. *et al.* Single-cell analysis reveals new evolutionary complexity in uveal melanoma.
682 *Nat Commun* **11**, 496 (2020). https://doi.org/10.1038/s41467-019-14256-1
683 36 Pelletier, J. & Sonenberg, N. Therapeutic targeting of eukaryotic initiation factor (eIF) 4E. *Biochem*
684 *Soc Trans* **51**, 113-124 (2023). https://doi.org/10.1042/bst20220285
685 37 Liu, X. L. *et al.* Emerging therapeutic strategies for metastatic uveal melanoma: Targeting driver
686 mutations. *Pigment Cell Melanoma Res* **37**, 411-425 (2024). https://doi.org/10.1111/pcmr.13161
687 38 Malina, A., Mills, J. R. & Pelletier, J. Emerging therapeutics targeting mRNA translation. *Cold*
688 *Spring Harb Perspect Biol* **4**, a012377 (2012). https://doi.org/10.1101/cshperspect.a012377
689 39 Grzmil, M. *et al.* MNK1 pathway activity maintains protein synthesis in rapalog-treated gliomas.
690 *The Journal of clinical investigation* **124**, 742-754 (2014). https://doi.org/10.1172/JCI70198

691 40 Kong, R., Qian, X. & Ying, W. Pancreatic cancer cells spectral library by DIA-MS and the
692 phenotype analysis of gemcitabine sensitivity. *Sci Data* **9**, 283 (2022).
693 https://doi.org/10.1038/s41597-022-01407-1
694 41 Li, J., Smith, L. S. & Zhu, H. J. Data-independent acquisition (DIA): An emerging proteomics
695 technology for analysis of drug-metabolizing enzymes and transporters. *Drug Discov Today*
696 *Technol* **39**, 49-56 (2021). https://doi.org/10.1016/j.ddtec.2021.06.006
697 42 Gyurkovska, V. *et al.* Dual function of Rab1A in secretion and autophagy: hypervariable domain
698 dependence. *Life Sci Alliance* **6** (2023). https://doi.org/10.26508/lsa.202201810
699 43 Wang, X. *et al.* Expression of Rab1A is upregulated in human lung cancer and associated with
700 tumor size and T stage. *Aging (Albany NY)* **8**, 2790-2798 (2016).
701 https://doi.org/10.18632/aging.101087
702 44 Thomas, J. D. *et al.* Rab1A is an mTORC1 activator and a colorectal oncogene. *Cancer Cell* **26**,
703 754-769 (2014). https://doi.org/10.1016/j.ccell.2014.09.008
704 45 Lu, Q., Wang, P. S. & Yang, L. Golgi-associated Rab GTPases implicated in autophagy. *Cell Biosci*
705 **11**, 35 (2021). https://doi.org/10.1186/s13578-021-00543-2
706 46 Kalirai, H., Dodson, A., Faqir, S., Damato, B. E. & Coupland, S. E. Lack of BAP1 protein
707 expression in uveal melanoma is associated with increased metastatic risk and has utility in routine
708 prognostic testing. *Br J Cancer* **111**, 1373-1380 (2014). https://doi.org/10.1038/bjc.2014.417
709 47 Sugase, T. *et al.* Development and optimization of orthotopic liver metastasis xenograft mouse
710 models in uveal melanoma. *J Transl Med* **18**, 208 (2020). https://doi.org/10.1186/s12967-020-
711 02377-x
712 48 Yang, X. Z. *et al.* Rab1 in cell signaling, cancer and other diseases. *Oncogene* **35**, 5699-5704
713 (2016). https://doi.org/10.1038/onc.2016.81
714 49 Pacheco-Fernandez, N., Pakdel, M. & Von Blume, J. Retention Using Selective Hooks (RUSH)
715 Cargo Sorting Assay for Protein Vesicle Tracking in HeLa Cells. *Bio Protoc* **11**, e3936 (2021).
716 https://doi.org/10.21769/BioProtoc.3936
717 50 Bartish, M. *et al.* The role of eIF4F-driven mRNA translation in regulating the tumour
718 microenvironment. *Nat Rev Cancer* **23**, 408-425 (2023). https://doi.org/10.1038/s41568-023-
719 00567-5
720 51 Xu, Y. *et al.* Translation control of the immune checkpoint in cancer and its therapeutic targeting.
721 *Nat Med* **25**, 301-311 (2019). https://doi.org/10.1038/s41591-018-0321-2
722 52 Viotti, C. ER to Golgi-Dependent Protein Secretion: The Conventional Pathway. *Methods Mol Biol*
723 **1459**, 3-29 (2016). https://doi.org/10.1007/978-1-4939-3804-9_1
724 53 Goldenring, J. R. A central role for vesicle trafficking in epithelial neoplasia: intracellular highways
725 to carcinogenesis. *Nat Rev Cancer* **13**, 813-820 (2013). https://doi.org/10.1038/nrc3601
726 54 Xu, S. *et al.* Function and regulation of Rab GTPases in cancers. *Cell Biol Toxicol* **40**, 28 (2024).
727 https://doi.org/10.1007/s10565-024-09866-5
728 55 Stenmark, H. Rab GTPases as coordinators of vesicle traffic. *Nat Rev Mol Cell Biol* **10**, 513-525
729 (2009). https://doi.org/10.1038/nrm2728
730 56 Goody, R. S., Müller, M. P. & Wu, Y. W. Mechanisms of action of Rab proteins, key regulators of
731 intracellular vesicular transport. *Biol Chem* **398**, 565-575 (2017). https://doi.org/10.1515/hsz-2016-
732 0274
733 57 Mughees, M., Chugh, H. & Wajid, S. Vesicular trafficking-related proteins as the potential
734 therapeutic target for breast cancer. *Protoplasma* **257**, 345-352 (2020).
735 https://doi.org/10.1007/s00709-019-01462-3
736 58 Jacob, A. *et al.* Rab40b regulates trafficking of MMP2 and MMP9 during invadopodia formation
737 and invasion of breast cancer cells. *J Cell Sci* **126**, 4647-4658 (2013).
738 https://doi.org/10.1242/jcs.126573
739 59 Zhang, L. *et al.* Rab25-Mediated EGFR Recycling Causes Tumor Acquired Radioresistance.
740 *iScience* **23**, 100997 (2020). https://doi.org/10.1016/j.isci.2020.100997

60 Morstein, J. *et al.* Targeting Ras-, Rho-, and Rab-family GTPases via a conserved cryptic pocket. *Cell* **187**, 6379-6392.e6317 (2024). https://doi.org/10.1016/j.cell.2024.08.017

61 Peng, C., Li, X., Ye, Z. & Wu, W. Rab1A promotes cell proliferation and migration by upregulating Gli1 in colorectal cancer. *Sci Rep* **11**, 16243 (2021). https://doi.org/10.1038/s41598-021-95798-7

62 Xu, X., Yin, K., Xu, S., Wang, Z. & Wu, R. Mass spectrometry-based methods for investigating the dynamics and organization of the surfaceome: exploring potential clinical implications. *Expert Rev Proteomics* **21**, 99-113 (2024). https://doi.org/10.1080/14789450.2024.2314148

63 Leung, K. K. *et al.* Broad and thematic remodeling of the surfaceome and glycoproteome on isogenic cells transformed with driving proliferative oncogenes. *Proc Natl Acad Sci U S A* **117**, 7764-7775 (2020). https://doi.org/10.1073/pnas.1917947117

64 Wang, C. *et al.* Regulation of Integrin β 1 recycling to lipid rafts by Rab1a to promote cell migration. *J Biol Chem* **285**, 29398-29405 (2010). https://doi.org/10.1074/jbc.M110.141440

65 Weidmann, C., Bérubé, J., Piquet, L., de la Fouchardière, A. & Landreville, S. Expression of the serotonin receptor 2B in uveal melanoma and effects of an antagonist on cell lines. *Clin Exp Metastasis* **35**, 123-134 (2018). https://doi.org/10.1007/s10585-018-9894-x

66 Le-Bel, G., Benhassine, M., Landreville, S. & Guérin, S. L. Analysis of the proteasome activity and the turnover of the serotonin receptor 2B (HTR2B) in human uveal melanoma. *Exp Eye Res* **184**, 72-77 (2019). https://doi.org/10.1016/j.exer.2019.04.013

67 Landreville, S. *et al.* Suppression of α5 gene expression is closely related to the tumorigenic properties of uveal melanoma cell lines. *Pigment Cell Melanoma Res* **24**, 643-655 (2011). https://doi.org/10.1111/j.1755-148X.2011.00869.x

68 Mouriaux, F. *et al.* Effects of Long-term Serial Passaging on the Characteristics and Properties of Cell Lines Derived From Uveal Melanoma Primary Tumors. *Invest Ophthalmol Vis Sci* **57**, 5288-5301 (2016). https://doi.org/10.1167/iovs.16-19317

69 Chen, P. W. *et al.* Expression of MAGE genes in ocular melanoma during progression from primary to metastatic disease. *Clin Exp Metastasis* **15**, 509-518 (1997). https://doi.org/10.1023/a:1018479011340

70 Labialle, S. *et al.* Characterization of the typical multidrug resistance profile in human uveal melanoma cell lines and in mouse liver metastasis derivatives. *Melanoma Res* **15**, 257-266 (2005). https://doi.org/10.1097/00008390-200508000-00005

71 Amirouchene-Angelozzi, N. *et al.* Establishment of novel cell lines recapitulating the genetic landscape of uveal melanoma and preclinical validation of mTOR as a therapeutic target. *Mol Oncol* **8**, 1508-1520 (2014). https://doi.org/10.1016/j.molonc.2014.06.004

72 Bérubé, M. *et al.* MMP-2 expression in uveal melanoma: differential activation status dictated by the cellular environment. *Mol Vis* **11**, 1101-1111 (2005).

FIGURES

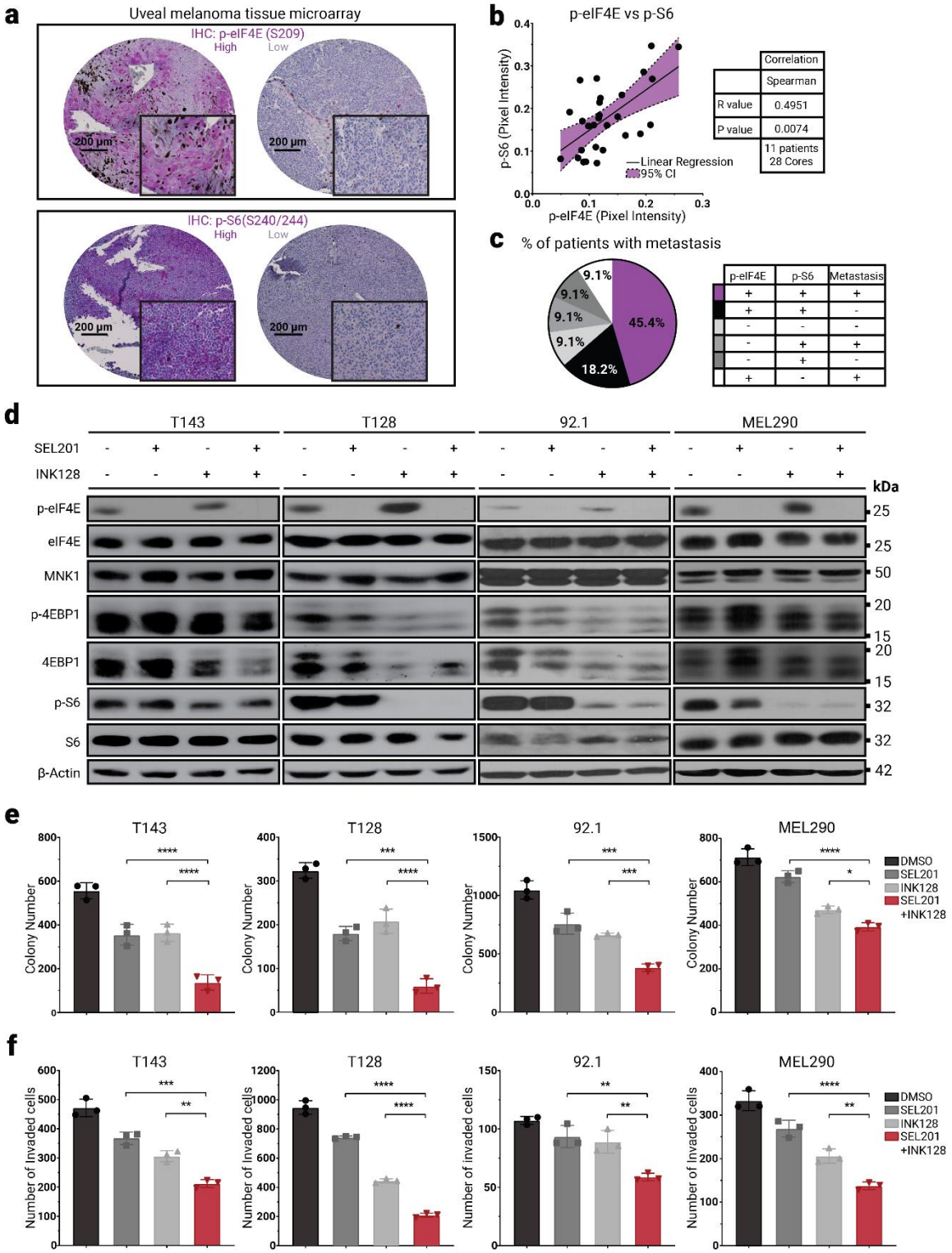

Fig. 1 | MNK1/2 and mTORC1/2 signaling is active in UM, where its co-targeting decreases clonogenic and invasive outgrowth *in vitro*. a, Representative images of immunohistochemistry (IHC) assays to detect p-eIF4E and p-S6 signaling status in human primary UM. Linear regression and 95% confidence

781 interval shown in purple. **b,** Spearman correlation performed on p-eIF4E and p-S6 tumor cores. **c,**
782 Proportion of patients (n=11) that developed metastases (+, -) categorized by p-eIF4E and p-S6 levels (+
783 high, - low). **d,** Immunoblot analysis of the indicated proteins in T143, T128, 92.1 and MEL290 UM cell
784 lines using 2.5μM SEL201 and 25nM INK128 inhibitors, alone or in combination. **e-f,** 2.5μM SEL201
785 cooperates with 25nM INK128 to decrease UM clonogenic outgrowth over 10 days and invasion over 24
786 hours of UM cell lines. Experiments represent the mean ±SD of 3 experimental replicates performed in
787 technical triplicate. One-way ANOVA multiple comparisons test. *$P \leq 0.05$, **$P \leq 0.01$, ***$P \leq 0.001$ and
788 ****$P \leq 0.0001$ compared to single treatments.

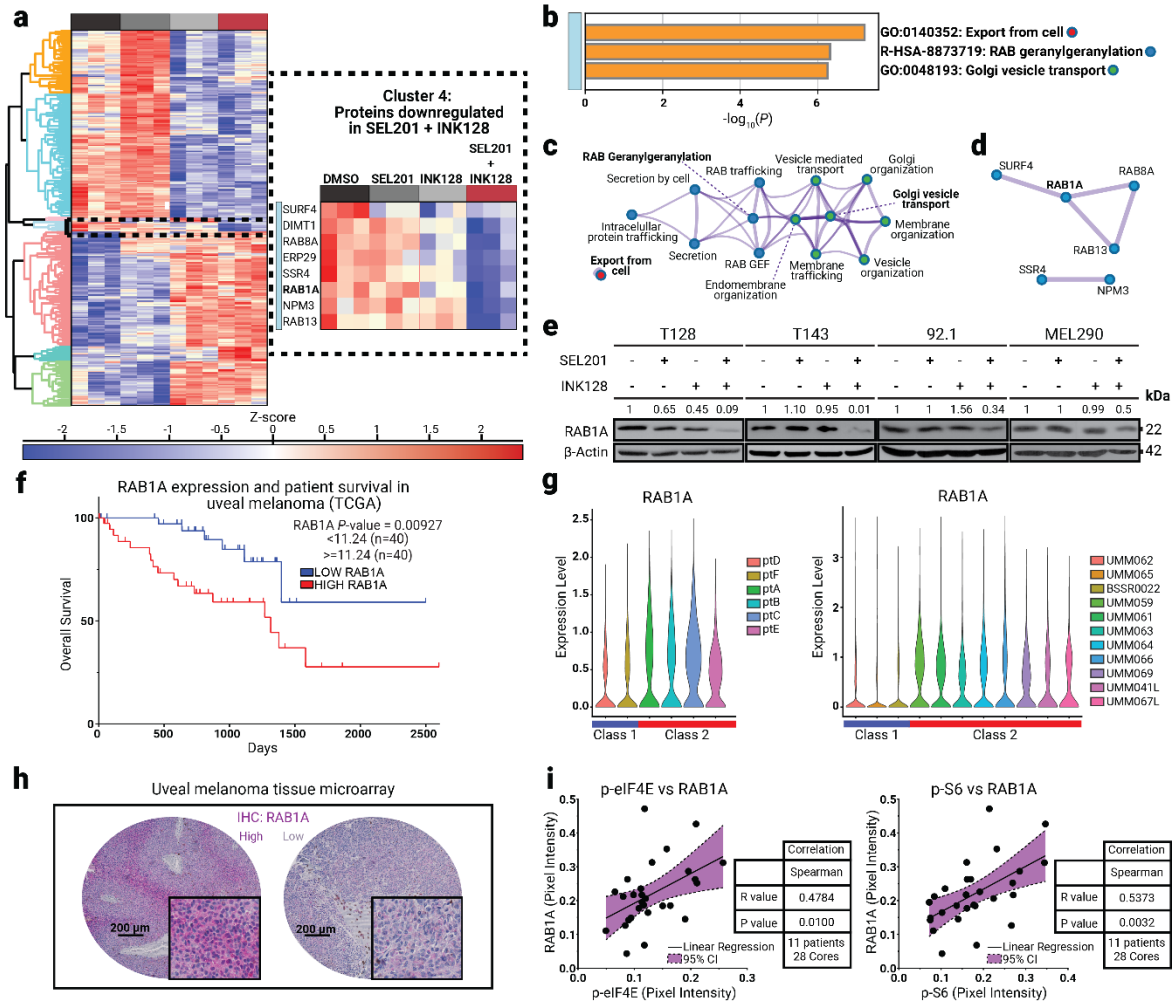

Fig. 2 | Proteome profiling of T128 UM cell line shows that combined inhibition of MNK1/2 and mTORC1/2 downregulates intracellular protein vesicle trafficking in UM. a, Heatmap of hierarchical clustering proteome of UM cells treated with vehicle, SEL201, INK128 or combination therapy at 24 h after treatment. **b-d,** Pathway Enrichment Analysis and protein-protein interaction of cluster 4 reveals the suppression of key proteins related to Golgi vesicle trafficking processes. **e,** Immunoblot validating that combined inhibition of the MNK-eIF4E and mTORC1/2-4EBP1 axes downregulates the expression of RAB1A in T143, T128, 92.1 and MEL290 UM cell lines at 24 hours after treatment. Densitometry values of RAB1A expression relative to DMSO are shown, normalized to β-actin. **f,** Kaplan-Meier overall survival plot depicting RAB1A mRNA expression in the TCGA UVM dataset (n=80), *P*-value=0.0092. **g,** Single cell RNA expression data from GEO #GSE138665 (left plot) and GEO #GSE139829 (right plot) shows RAB1A expression in Class 1 and 2 UM samples. **h,** Representative images of immunohistochemistry to detect RAB1 expression in human UM. **i,** Spearman correlation performed on RAB1A vs p-eIF4E (left) and RAB1A vs p-S6 tumor cores (right). Linear regression and 95% confidence interval shown in purple.

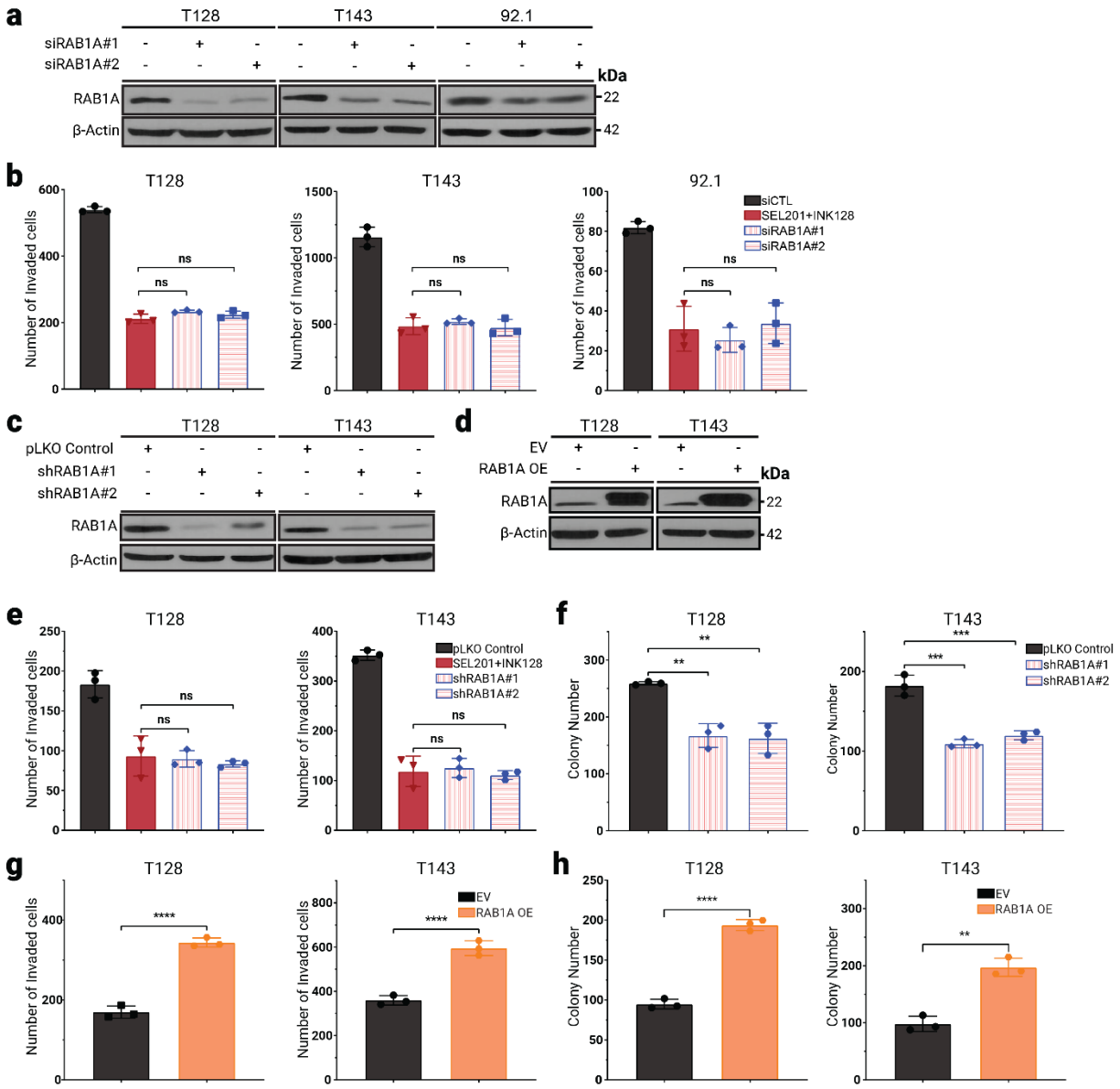

Fig. 3 | RAB1A expression influences invasive and clonogenic potential of T128 and T143 UM cell lines. a, Immunoblot of T128, T143, and 92.1 transfected with control treatment or transient siRNA against RAB1A. **b,** RAB1A transient knockdown decreases invasion in T128, T143 and 92.1, comparable to the effect observed under combined MNK1/2-mTORC1/2 pharmacological inhibition. Experiments represent the mean ±SD of 3 experimental replicates performed in technical triplicate. One-way ANOVA multiple comparisons test, ns=non-significant compared to combination treatment. **c,** Immunoblot of T128 and T143 transduced with stable shRNA (shRNA#1&2) against RAB1A compared to pLKO Control. **d,** Immunoblot of RAB1A expression in T128 and T143 cell lines transfected with empty vector (EV) or plasmid encoding human RAB1A (RAB1A OE). **e-f,** RAB1A stable knockdown mimics MNK1/2-mTORC1/2 pharmacological inhibition to decrease invasion and clonogenic outgrowth on T128 and T143 cell lines. Experiments represent the mean ±SD of 3 experimental replicates performed in technical triplicate. One-way ANOVA multiple comparisons test, ns=non-significant, *$P \leq 0.05$, **$P \leq 0.01$, ***$P \leq 0.001$, ****$P \leq 0.0001$ compared to combination. **g-h,** RAB1A overexpression enhances clonogenic and invasive

815 potential of T128 and T143 compared to EV. Experiments represent the mean ±SD of 3 experimental
816 replicates performed in technical triplicate. Unpaired t-test, $^{**}P \leq 0.01$, $^{****}P \leq 0.0001$ compared to EV.

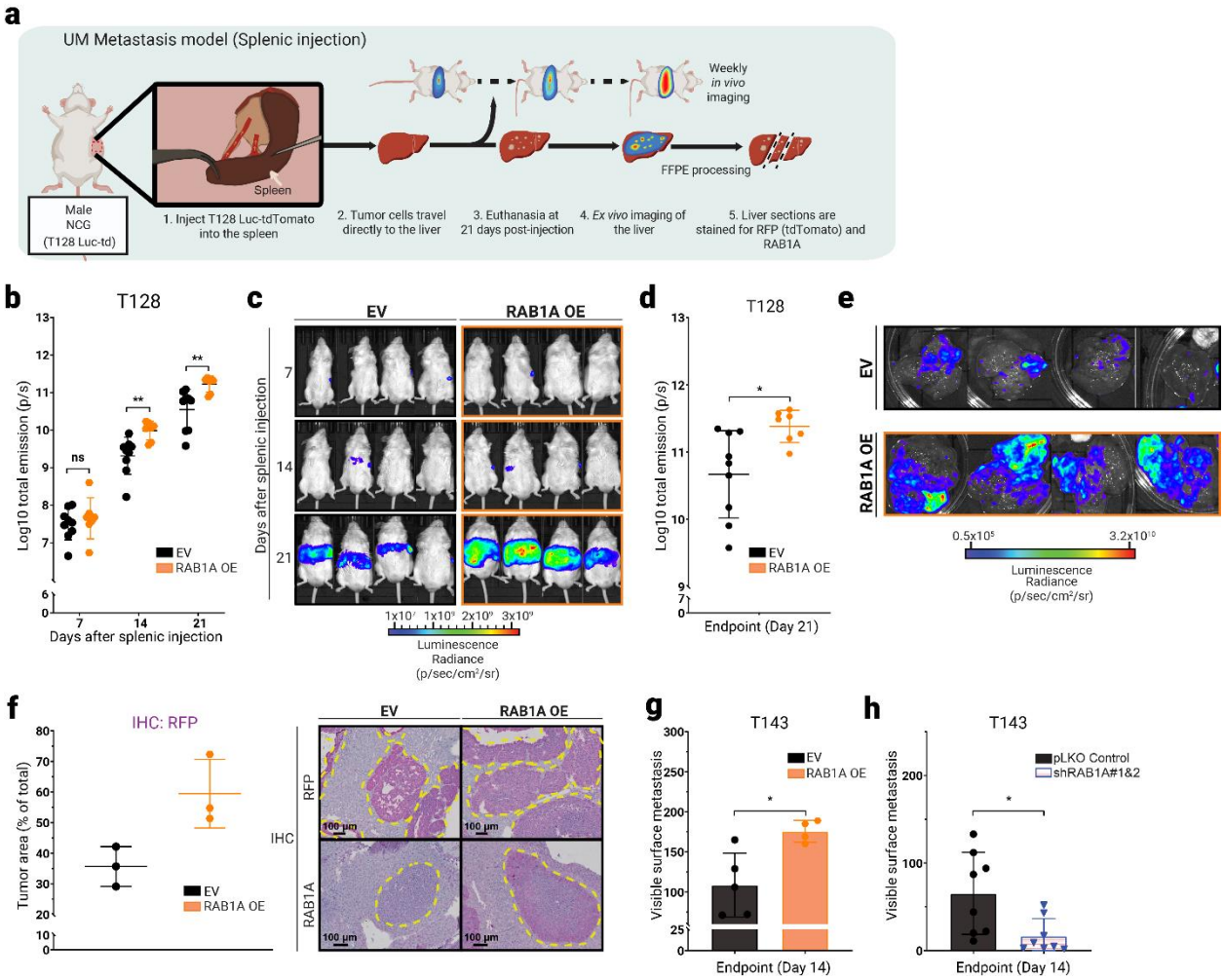

Fig. 4 | RAB1A expression modulates *in vivo* metastasis potential of T128 and T143 UM cell lines. a, Splenic injection model diagram using NCG mice injected with T128 luc-tdTomato or T143. Tumor burden (T128) was determined by log10 luminoscore (photons/sec) acquired weekly and using surface metastasis (T143) on NCG livers. **b-c,** *In vivo* imaging and representative images at each timepoint of NCG bearing T128 luc-tdTomato tumors transduced with EV (n=9) and RAB1A OE (n=7), Multiple t-test analysis. ***P* ≤0.005 at day 14 and 21. **d-e,** *Ex vivo* imaging and representative images of NCG livers with T128 luc-tdTomato EV or RAB1A OE tumors, Mann-Whitney test analysis. **P* ≤0.05. **f,** Representative images and quantification of red fluorescent protein (RFP) IHC on T128 metastasis-bearing livers. Area noted in yellow corresponds to T128 liver metastasis. **g-h,** Quantification of surface liver metastasis of NCG mice intrasplenically injected with the T143 cell line that overexpresses RAB1A (n=4), EV (n=5), expresses RAB1A shRNA (n=8) or pLKO Control (n=8), Mann-Whitney test analysis. **P* ≤0.05.

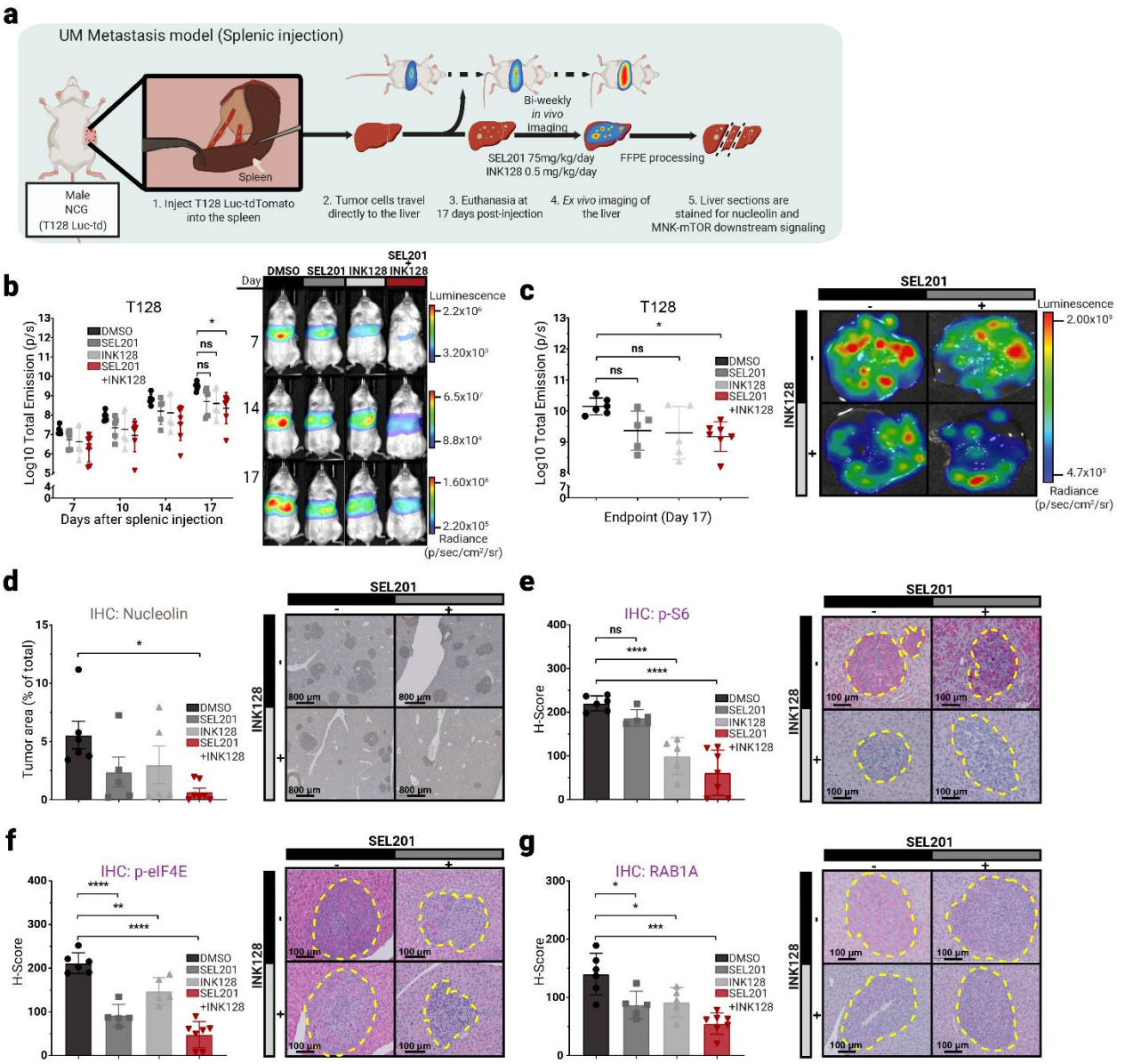

Fig. 5 | MNK1/2 and mTORC1/2 pharmacological inhibition reduces T128 liver metastasis *in vivo*. a, Schematic overview of the splenic injection model using NCG mice injected with T128 luc-tdTomato; the tumor burden was determined by log10 luminoscore (photons/sec) acquired bi-weekly. NCG mice were treated with vehicle, SEL201 (75 mg/kg per day) and INK128 (0.5 mg/kg per day). **b,** *In vivo* imaging of NCG bearing T128 luc-tdTomato tumors treated with vehicle (n=6), SEL201 (n=5), INK128 (n=5) and combination treatments (n=7), two-way ANOVA multiple comparisons test, ns=non-significant, *$P \leq 0.05$ at day 17. **c,** *Ex vivo* imaging of NCG with T128 luc-tdTomato metastases treated with vehicle (n=6), SEL201 (n=5), INK128 (n=5) and combination treatments (n=7), one-way ANOVA multiple comparisons test, ns=non-significant, *$P \leq 0.05$. **d-g,** Representative images and quantification of human nucleolin for metastasis area (detection using DAB), p-S6, p-eIF4E and RAB1A (detection using Magenta) IHC of NCG livers injected with T128 luc-tdTomato. One-way ANOVA multiple comparisons test, ns=non-significant, *$P \leq 0.05$, **$P \leq 0.01$, ***$P \leq 0.001$ and ****$P \leq 0.0001$. Areas noted in yellow correspond to T128 liver metastasis.

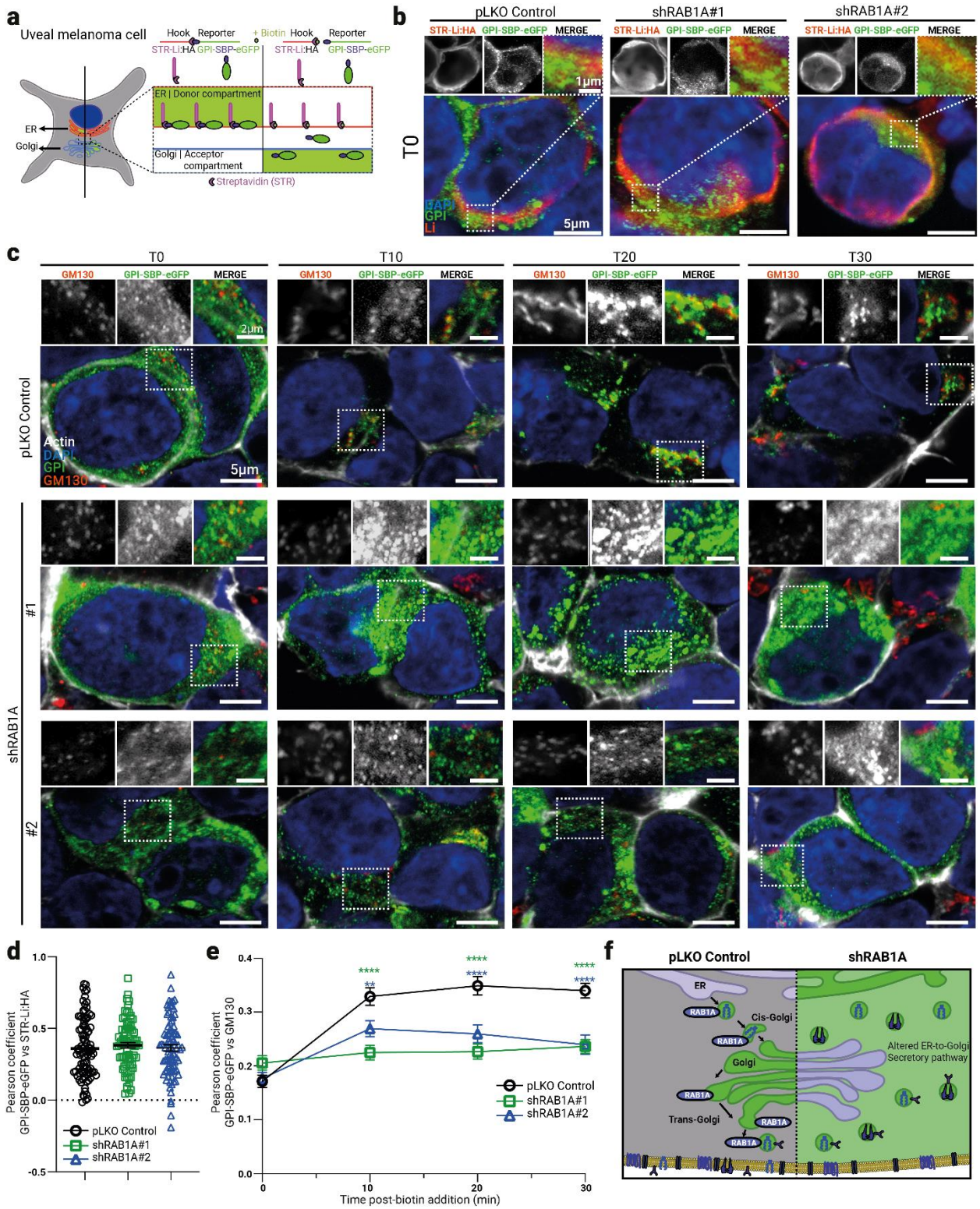

Fig. 6 | RAB1A depletion impairs the ER-to-Golgi secretory pathway. a, Schematic overview of the RUSH assay imaging on T128 UM cell lines (pLKO and shRAB1A#1/2). Cells are transiently transfected with a plasmid containing the hook (STR-Li: HA) and the reporter (GPI-SBP-eGFP). Newly synthesized reporters are retained in the ER (donor compartment) by the hook, once biotin is added to the medium,

845 reporters are released into the cytoplasm, allowing them to resume its trafficking to the Golgi. **b,**
846 Representative confocal images of cargo protein (GPI-SBP-eGFP, green) distribution and ER anchor
847 protein (STR-Li:HA, red) prior to the addition of biotin (T0) in T128 cells. Single channels for Li and GPI
848 are shown above the magnification of the boxed area displayed in the upper-right panel. **c,** Representative
849 confocal images of cis-Golgi (GM130, red) and cargo protein GPI-SBP-eGFP (green) at 0-, 10-, 20-, or 30-
850 minutes post-addition of biotin to the culture medium. Individual and merged channels of the magnified
851 boxed area are shown above each image. **d,** Pearson coefficient correlation of STR-Li:HA and GPI-SBP-
852 eGFP in c. **e,** Pearson coefficient correlation of GM130 and GPI-SBP-eGFP at each timepoint of the RUSH
853 assay. b, d: n=3 for pLKO Control, shRAB1A#1 n=3, shRAB1A#2 n=3. c, e: n=3. Error bars represent the
854 mean ± S.E.M. One-way or two-way ANOVA with Dunnett post-comparison test was performed to compare
855 RAB1A KD cells to the control. **f,** Schematic describing the effect of decreased RAB1A expression on the
856 secretory pathway, where it shows the improper localization of cargoes through the cytoplasm using the
857 RUSH assay.

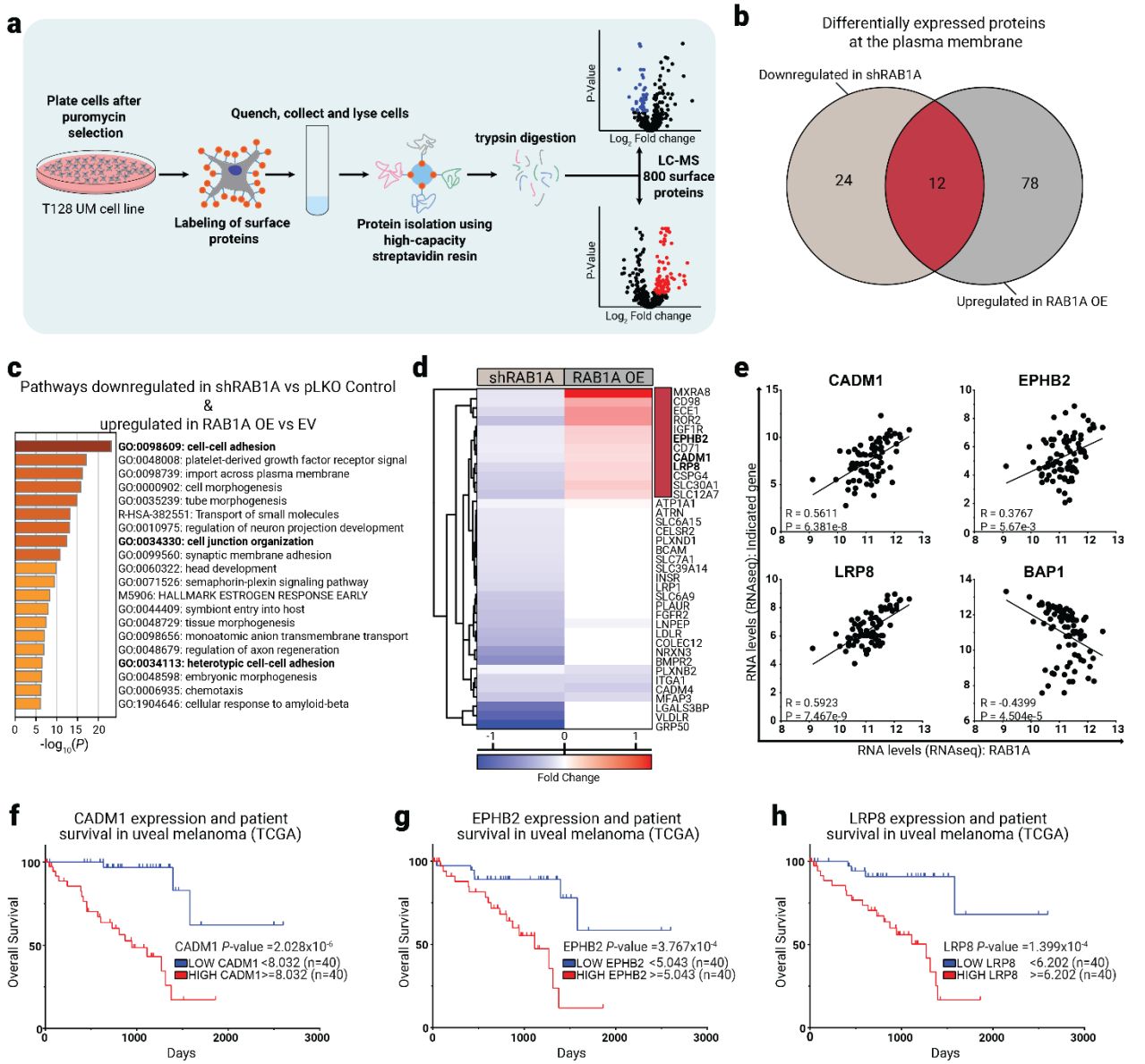

Fig. 7 | Surfaceome profiling of UM cells with altered RAB1A expression uncovers novel druggable targets. a, Schematic of the methodology followed to determine protein expression at the cell surface in T128 RAB1A OE, EV, shRAB1A and pLKO Control UM cell lines. LC-MS: Liquid chromatography mass spectrometry. **b,** Venn diagram describing the number of differentially expressed proteins at the cell membrane between the indicated cell lines. **c,** Pathway enrichment analysis of proteins at the cell membrane found to be downregulated in **b** shRAB1A vs pLKO Control and upregulated in RAB1A OE vs EV. **d,** Heatmap of hierarchical clustering of proteins downregulated in shRAB1A and upregulated in RAB1A OE at the cell membrane. **e,** Correlation of RAB1A RNA expression with the RNA expression of the listed gene. Spearman-rank order, linear regression shown. **f-h,** Kaplan-Meier overall survival plots depicting CADM1, EPHB2, LRP8 and BAP1 expression in the TCGA UVM dataset (n=80).